International Journal of Innovative
Computing, Information and Control
Volume **19**, Number **3**, June **2023**

ICIC International ©2023 ISSN 1349-4198
pp. **737–762**

OUTPUT FUSION OF MPC AND PID AND ITS APPLICATION IN INTELLIGENT LAYERED WATER INJECTION OF OILFIELD

Yuanlong Yue[1,*], Haoyang Wen[1], Xin Zuo[1], Mao Sheng[2] and Fuchao Sun[3]

[1]College of Information Science and Engineering
[2]College of Petroleum Engineering
China University of Petroleum (Beijing)
No. 18, Fuxue Road, Changping District, Beijing 102249, P. R. China
2020211243@student.cup.edu.cn; {Zuox; Shengmao}@cup.edu.cn
[*]Corresponding author: yueyuanlong@cup.edu.cn

[3]Research Institute of Petroleum Exploration and Development
No. 31, Xueyuan Road, Haidian District, Beijing 100083, P. R. China
fuchao.sun@petrochina.com.cn

Received October 2022; revised February 2023

Abstract. *Efficient and reliable wireless wave-code communication technology is crucial for improving the efficiency of intelligent stratified water injection in oilfield; however, the existing technology suffers from slow wave-code generation and low wave-code recognition rate due to the poor fluid-driven control method of pipe column. In order to improve the dynamic response performance of wave code communication, this paper proposes an output fusion optimal control method based on MPC-PID (Multivariable Predictive Control-Proportional Integral Derivative Control). Firstly, the dynamic response characteristics of well structure and formation flow-pressure characteristics with whole-well water distribution equipment are analyzed, and secondly, the wave code generation models of whole-well and different layer sections of stratified water injection are established by combining the whole-well structure and physical dynamic processes. Finally, the MPC-PID optimal fusion control algorithm is designed and the calculation process of the optimal weights is presented. The simulation results show that the MPC-PID fusion control method is superior to the traditional method in reducing overshoot, stability, and robustness, which effectively improves the efficiency of wave-code communication.*
Keywords: Weighted fusion control, Layered intelligent water injection, Dynamic performance optimization, Optimal weight distribution, Multivariate predictive control

1. **Introduction.** The supply conflict of petroleum energy in today's world is becoming increasingly prominent, and how to improve the recovery ratio with the existing proven reserves is becoming an issue of growing importance [1]. Artificial oil drive technology is an effective means to increase production in oilfield production, and the existing efficient oil drive methods mainly include carbon dioxide drive, chemical drive, nano flooding, water drive [2-4], but water drive is still the most widely used technology due to the limitation of cost and research level [5-7]. However, the normal water drive method does not apply to current tight reservoirs with a high reserve share and wide geographic distribution [8,9], because of the high opening pressure of such reservoirs [10], complex geological conditions, and obvious differences in physical properties such as pore structure and denseness of rocks in each layer section [11], so it is harder to maintain a full well water injection qualification rate using the traditional water drive method, which leads to unrealized single well target production and thus lower economic efficiency [12]. The traditional water injection method

DOI: 10.24507/ijicic.19.03.737

uses generalized co-injection and uses armor or steel pipe cables for communication, with low extraction quality and safety risks during testing. In contrast, in single-well multi-layer segment injection operations, for layers with a certain permeability, when the flow does not reach optimal values, it leads to insufficient pressure and reduced recovery, which indirectly reduces the efficiency of energy use. However, oversized flow can lead to layer pressure overload, harming the geological structure of the layer segment, causing single layer bursts and ineffective water circulation, and a dramatic increase in water content [13], so it is crucial to keep the flow values of the layer segment matching the optimal value [14]. To this end, the layered segment fine water injection technology was developed, which independently sets mining parameters according to the geological characteristics of different layers, effectively solving the problems of inter-layer interference and uneven flow advance [15], thus realizing the optimal control of pressure and flow in the layers and ensuring the recovery rate of the layers with different characteristics [16].

In layered water injection operations, the reservoirs are buried deeper in the ground and the injection status parameters are more difficult to obtain, making it impossible to achieve real-time monitoring of the underground water injection status. Therefore, it is crucial to realize the transmission communication between the wellhead and the well. Existing technologies use interoperable cables for communication. In 2019, Zhou applied the layered water injection technology based on preset cables experimentally in Daqing oilfield [17], which effectively reduced the cost of manual well logging, realized real-time monitoring of downhole data, and improved the qualification rate of layered water injection. However, it is obvious that this technique of cable repair is inconvenient and the maintenance cost is high [18]. In 2020, Tong studied the wireless intelligent water injection technology based on a computer network [19], which uses PID algorithm to control the water distribution flow, compared with cable transmission whose advantage is that it does not require larger upfront investment and cable maintenance, the disadvantage is that wireless communication is not timely, more dependent on network communication, while the control algorithm is simple and cannot meet the dynamic performance requirements of flow control in different layer sections. In 2020, a wave code communication technology was proposed [20], which decodes and converts fluid fluctuation signals into control signals to achieve this. This technology uses fluid as the signal medium, which effectively solves the problems of difficult protection and the high operating cost of traditional intelligent layered water injection communication equipment. However, the use of simple control algorithms for flow regulation generates many wave code transmission links and long delays, resulting in slow pressure response and high symbol error rates, which cannot meet the needs of efficient decoding, fast following of target values, and real-time communication, resulting in power wastage and actuator wear. All in all, the study of advanced control algorithms for intelligent water injection control of complex layer segments has high economic efficiency and applicability.

Layered water injection is a typical multivariate coupling process, which requires the design of targeted control methods. Model predictive control (MPC), as a commonly used advanced control algorithm, has certain inherent decoupling capabilities, and its control law is based on the characteristics of the model, making its control specialization better than PID control algorithms. However, for variable objects that require fast response such as flow, the response speed, and anti-interference characteristics will not meet the requirements due to their calculation speed [21]. In addition, the model predictive control algorithm is more complex and the parameters are more inconvenient to adjust, so it is generally used as a master controller in conjunction with proportional-integral control. Therefore, Ravendra et al. proposed an MPC-PID cascade control algorithm for the pharmaceutical process [22] and performed process simulation of direct tablet pressing

process using gPROMS software. The results showed that the product qualification rate was significantly improved compared to the string-level PID control algorithm and the MPC algorithm alone [23]. Its use of MPC output to do the main loop set value, PID controller as the lower-level controller determines the main dynamic performance of the system, compared to the PID control quality improved. However, the output overshoot is still large, and the oscillation cannot be eliminated. Meanwhile, the direct introduction of PID will weaken the robustness of MPC, in the case of large model gain coefficient and mismatch will seriously deteriorate the system performance.

In order to effectively improve the performance of a single traditional control algorithm, simple control algorithms driven by parameter optimization methods have been widely studied, among which control strategies based on data-driven and fusion of control laws have achieved positive results. In 2013, Ni proposed the integral-fusion-Smith fusion control algorithm [24], which overcomes the weaknesses of the system with large time lag and difficulty in control when the model is mismatched, and its control accuracy is high and the dynamic performance index of the system is improved while showing better robustness. In 2019, a control strategy using genetic algorithm to optimize PID controller parameters was proposed by Chen et al. [25] and achieved promising stability in the control task of semi-active suspension of vehicles under different road conditions. In 2021, Zhuang and Zhu presented a fractional-order internal mode controller based on neural network self-tuning to control the temperature of AC rooms [26], which reduced the control overshoot and steady-state time. In 2022, Kurokawa et al. proposed a data-driven regulator PID control method based on model-referenced robust rectification [27]. This algorithm optimizes the PID controller parameters, enhances the disturbance rejection performance, and achieves a trade-off design between robust stability and regulator performance. In 2020, Deng et al. proposed a weighted fusion algorithm of fuzzy PID control and active disturbance rejected control (ADRC) for the optimal control of proton exchange membrane fuel cells (PEMFC) [28], the results show that the response overshoot and error become smaller, and the immunity of the system is greatly improved, solving the problem of insufficient oxygen during sudden load changes. In the proposed algorithm, MPC is placed in the outer loop of the algorithm, which improves the delay processing capability and robustness of the system, and the PID cascade link in the inner loop is responsible for improving the response speed and enhancing the ability to resist sudden disturbances, and the two are fused with optimal weights so that the optimization effectiveness of the dual algorithms can reach the optimal equilibrium state and achieve fast and accurate control.

The main innovations and contributions of this paper are summarized as follows.

1) The relationship between differential pressure and flow rate under complex wellbore space structure is analyzed, and a steady-state working point model is established to solve the amplitude problem of wave code. In addition, the dynamic characteristics of the water distribution equipment are taken into account, and a dynamic mathematical model of fluid fluctuation is established to complete the dynamic description of the wave code generation process.

2) The design flow of the fusion controller is described in full in the paper. Through the analysis of the fusion process and the transformation of the model structure, the output control law is calculated, and the calculation of the optimal weights is given by integrating the response characteristics.

2. **Layered Water Injection Modeling.**

In this section, a steady-state model of the layered intelligent water injection process is established by combining actual working conditions. A single-well layered water injection model is considered, consisting of N

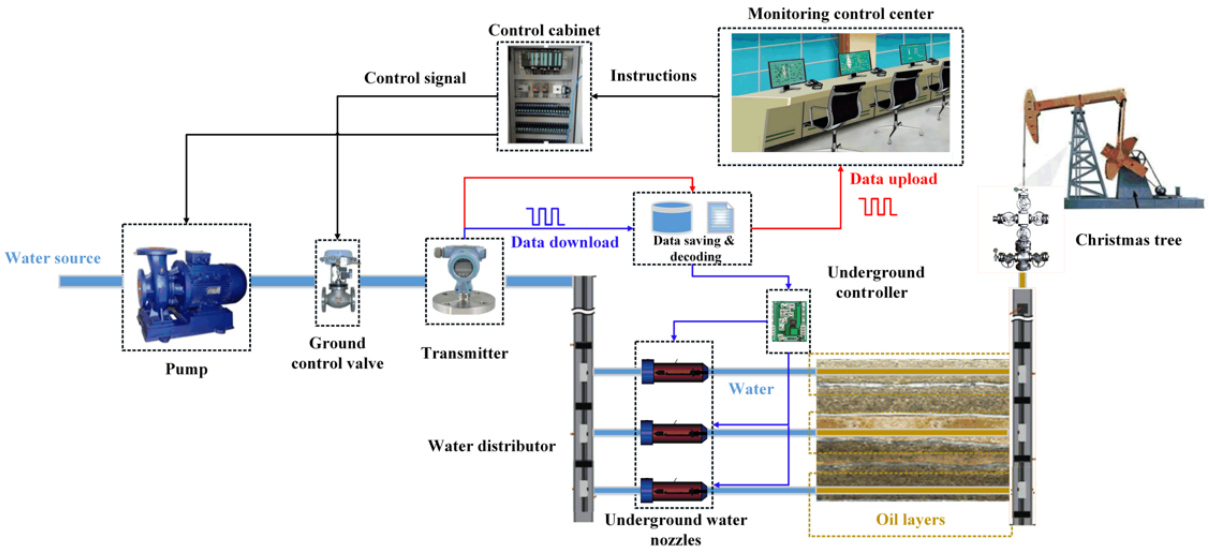

FIGURE 1. Schematic diagram of the overall architecture of the intelligent layered water injection system

layers with different geological characteristics and a layered water injection control system, which includes ground control valves, water distributors with water nozzle groups set underground, water injection packer, pumping machines, a central control system, etc. [29]. Accordingly, the overall architecture of the intelligent layered water injection system is shown in Figure 1.

As shown in the figure, in the intelligent injection distribution system, wave code communication between the wellhead and the underground distributor is carried out through periodic adjustment of the regulating valve. In the data upload stage, the underground water nozzle cyclically changes the opening degree and transmits the fluctuation information of relevant physical quantities to the database through sensors, which is retrieved and decoded by the monitoring center to obtain the downhole layered water injection parameters to judge the working status of the well accordingly. During the data transmission stage, the user sends instructions to control the ground valve group, corresponding to the generation of periodic fluctuation data information, which is decoded and transmitted to the underground controller loaded with control algorithms that drives the water distributor to finely adjust the spout opening degree for intelligent flow control. The user can set the parameters of the pump and controller in the ground control center during the operation.

Next, the pressure-flow characteristics during stratified water injection are analyzed: the pressure-flow characteristics of the Nth layer are described using the following relationship.

$$p_{(N)} = k_{(N)} q_{v(N)} + b_{(N)} \tag{1}$$

k is inversely proportional to the layer permeability and b indicates the initial opening pressure of the layer. The flow is allowed to be injected into the layer when the external pressure is greater than this value [30-32]. From the layer properties, it is known that full well fracturing can be achieved when the pump pressure is greater than the opening pressure of all layers. This leads to

$$P_0 \geq b_{(t)\max}, \quad t = 1, 2, \ldots, N \tag{2}$$

The low limit of the full well flow at this point can be obtained as

$$Q_{0l} = \sum_{i=1}^{N} \frac{C_{(i)}\sqrt{{C_{(i)}}^2 {k_{(i)}}^2 - 4\left(b_{(i)} - b_{(t)\max}\right)} - {C_{(i)}}^2 k_{(i)}}{2} \tag{3}$$

Entering the water injection adjustment process and studying the equivalent steady-state modeling method between the incoming water at the wellhead and the layer section, it is necessary to specify the steady-state pressure-flow operating point under different equipment parameters. Set the ith layer section nozzle opening from $C_{(i)0}$ to $C_{(i)}$, the jth layer flow steady state value becomes $q_{v(ij)}$, the downhole post-valve pressure is P, the incoming water pressure is P_0, and the ground control valve opening is C_0. Firstly, the differential pressure-flow relationship of the wellhead section is listed as

$$P = P_0 - \frac{\left(\sum_{j=1}^{N} q_{v(ij)} + q_{v(i)}\right)^2}{{C_0}^2}, \quad \{j \neq i\} \tag{4}$$

Extend the above differential pressure-flow relationships to the full well:

$$\begin{cases} q'_{v(i)} = \dfrac{C_{(i)}\sqrt{{C_{(i)}}^2 {k_{(i)}}^2 - 4\left(b_{(i)} - P\right)} - {C_{(i)}}^2 k_{(i)}}{2} \\ q'_{v(ij)} = \dfrac{C_{(j)}\sqrt{{C_{(j)}}^2 {k_{(j)}}^2 - 4\left(b_{(j)} - P\right)} - {C_{(j)}}^2 k_{(j)}}{2} \end{cases} \tag{5}$$

Flow values should be required to meet all layer opening and pressure limiting conditions:

$$\begin{cases} \max\left(Q_{0l}, Q'_{0l}\right) \leq \sum_{i=1}^{N} q_{v(ij)} + q_{v(i)} < 2C_0\sqrt{P_m - b_{(t)\min}} \\ q_{v(i)0}, q_{v(i)} < C_0\sqrt{P_m - b_{(i)}},\ q_{v(ij)} < C_0\sqrt{P_m - b_{(j)}} \end{cases} \tag{6}$$

where C is the nozzle throttling coefficient:

$$C = \frac{\pi d^2 C_m}{4}\sqrt{\frac{2}{\rho\left(1 - \bar{\beta}^2\right)}} \tag{7}$$

C_m is the nozzle circulation parameter, depending on its selection specifications [33], $\bar{\beta}$ is the spool circulation area ratio under the steady-state operating point, ρ is the fluid density, with d being the internal diameter of the pipeline. According to the above steady-state model and Table 1 of layer characteristics parameters, the relationship curves between the pressure after the valve P and the flow of each layer section or the flow of the whole well shown in Figure 2.

The curve in the figure is generated by connecting the points of the whole well. When the system is at the continuous operating point, the nozzle action is extremely slow and each dynamic process cycle is extremely short, so the pressure and flow value changes

Table 1. Table of layer parameters

Item	**Water absorption index (k^{-1})** $\mathbf{m^3{\cdot}h^{-1}{\cdot}MPa^{-1}}$	**Opening pressure (b)** **MPa**	**Opening ($\bar{\beta}$)** **%**
1	2.23	1.35	35
2	1.12	2.07	50
3	3.96	3.45	60

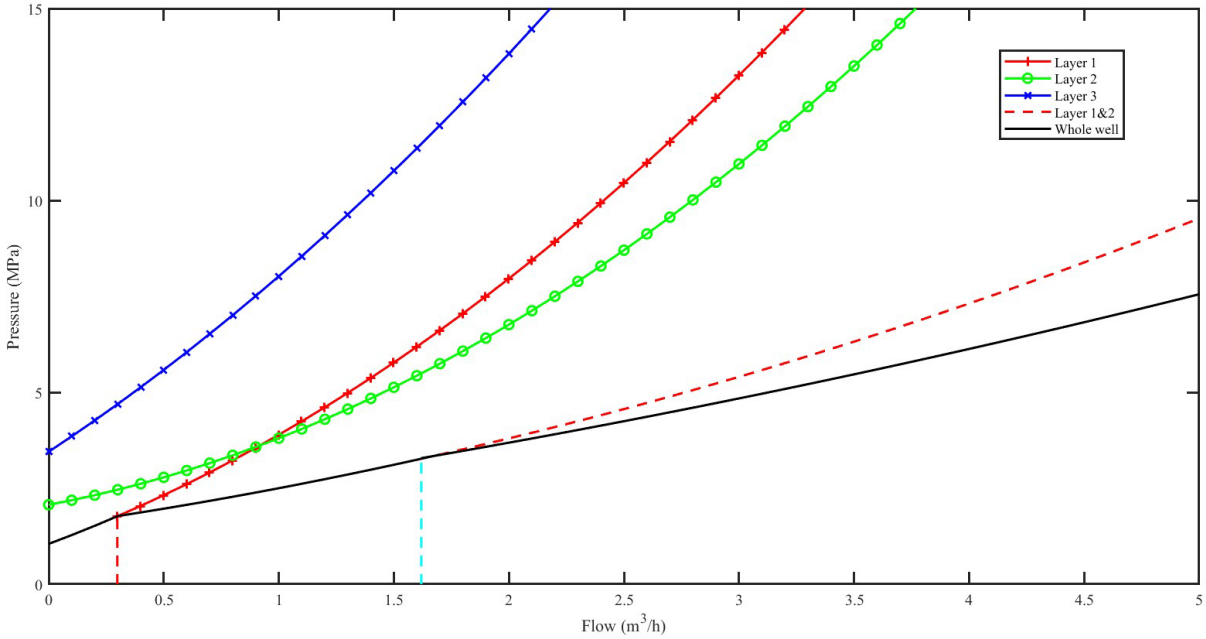

FIGURE 2. Simulation results of post-valve pressure versus flows

can be regarded as steady-state processes. The colored curves show the pressure-flow relationship for each layer segment, while the black curve at the bottom represents the full well flow versus pressure with openness during a steady state. From the figure, it can be seen that the curve of the high permeability layer is flatter, its flow value varies more under the same change of opening degree, and the injection efficiency is higher. As the post-valve pressure increases, the high opening pressure layer section begins to meet the conditions for injection flow, so the full well flow-pressure curve shows a segmented trend, and the trend becomes smoother, while the wave code communication becomes more difficult. Therefore, in practice, to maintain the water injection qualification rate of low-permeability reservoirs while ensuring the effectiveness of wave code communication in each layer, it is necessary to close the water nozzles of certain high-permeability layers to balance the flow between layers. In wave code communication, the underground water distributor drives the underground nozzle opening degree to change periodically, generating wave code to complete the data upload operation. The fluctuation range of nozzle opening in the selected 2-layer section is 50%-75%, corresponding to the pressure-flow relationship curve after the valve as shown in Figure 3.

The above model describes the steady-state pressure-flow operating point of stratified water injection. Next, the dynamic generation process of wave code is studied by combining the actuator characteristics and wave code transmission characteristics, and the dynamic model of fluid fluctuation under fast control of water distributor is established. Considering the working conditions of fixed valve opening at the surface wellhead and downhole water distributor driving water outlet manifold regulation, to clarify the specific dynamic process of regulation, the dynamic flow response characteristics of single seat valve action in layer i section are described as follows:

$$m\ddot{q}_{pe(i)}(t) + \mu\dot{q}_{pe(i)}(t) + \varepsilon q_{pe(i)}(t) = K_{v(i)}\beta_{(i)}(t)F_{m(i)}(t-\tau_c) \tag{8}$$

q_{pe} is the relative flow and K_v is the gain factor derived from the valve's algebraic flow characteristics of the valve.

$$K_v = R^{\left(\bar{\beta}^{-1}-1\right)} \ln R \tag{9}$$

R is the adjustable ratio of nozzle flow, m, ε are the mechanical parameters associated with the nozzle valve body, μ is the coefficient of friction of media viscosity, β is the flow ratio of the nozzle, and F_m is the spool force when the controller signal is fully loaded. τ_c is the delay time of valve movement, which is related to the nozzle stem turning angle speed and signal transmission delay. The above relationship is combined to obtain the steady-state flow operating point of the layer whose nozzle acts, which leads to the full process characteristic model of this layer as the following equation:

$$m\ddot{q}_{v(i)}(t) + \mu\dot{q}_{v(i)}(t) + \varepsilon q_{v(i)}(t) = K_{v(i)}q_{v(i)}\beta_{(i)}F_{m(i)}(t-\tau_c) \tag{10}$$

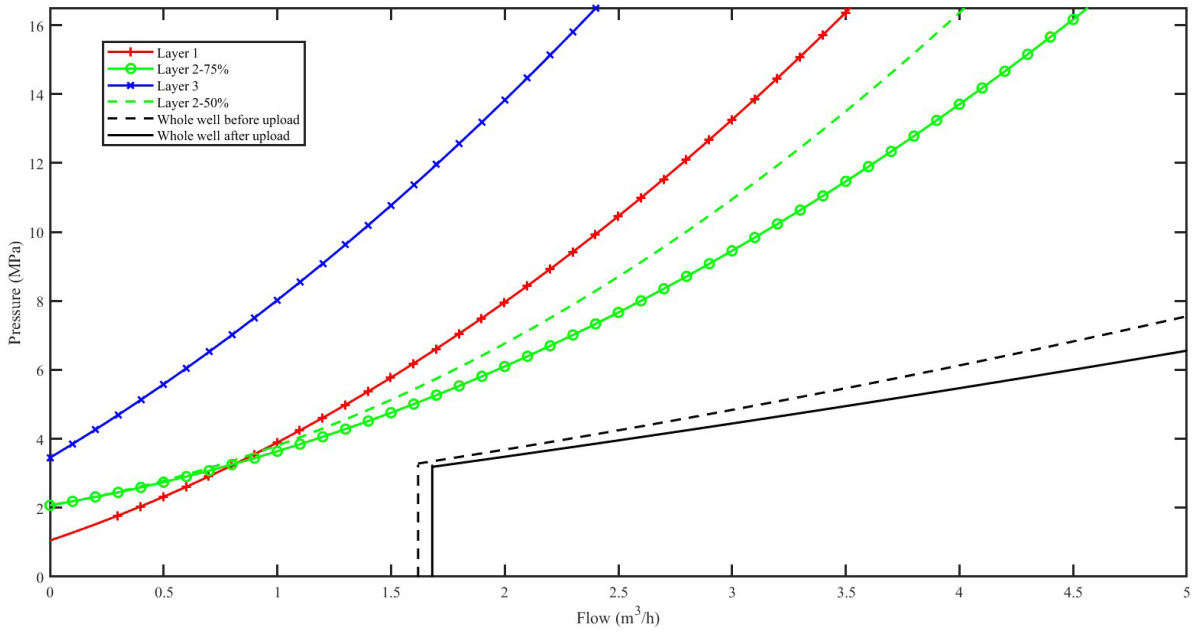

FIGURE 3. Simulation results of post-valve pressure and flow rate for data upload conditions

In addition, due to the fact that the different pipeline flow in a layer nozzle action will produce interlayer mutual disturbance effect, according to the principle of flow mutual disturbance process, the relative flow q_{pe} is directly related to disturbance target layer's nozzle opening degree $\beta_{(j)}$, and the entire action process $\beta_{(j)}$ is constant, so the reciprocal layer section flow change is essentially achieved by changing the pressure after the valve P. Changes in flow or pressure will be propagated to other layers after a certain period in the form of energy waves.

Set the wave code water strike propagation velocity to v, which is related to the pipe diameter, signal frequency, and other parameters. Set l_e as the unit tube length, the difference in well depth between neighboring layers is h_d, and then the dynamic process model for the action of a single-layer section nozzle on the output of the jth layer section is described as follows:

$$\begin{aligned}&\left[m\ddot{q}_{v(ij)}(t) + \mu\dot{q}_{v(ij)}(t) + \varepsilon q_{v(ij)}(t)\right]\left[l_e\dot{q}_{v(ij)}(t) + vq_{v(ij)}(t)\right]\\ &= vK_{v(j)}q_{v(ij)}\beta_{(j)}F_{m(j)}(t-\tau_c-\tau_l)\end{aligned} \tag{11}$$

τ_l is the path delay for wave code transmission:

$$\tau_l = |i-j|\tau_e, \quad \tau_e = \frac{h_d}{v} \tag{12}$$

Extend the above dynamic model into a state-space form as

$$\begin{aligned}\dot{\boldsymbol{x}}_{\boldsymbol{m}} &= \boldsymbol{diag}(\boldsymbol{A}_{\boldsymbol{me}})\boldsymbol{x}_{\boldsymbol{m}} + \boldsymbol{diag}(\boldsymbol{B}_{\boldsymbol{me}})\boldsymbol{u} \\ \boldsymbol{y}(k) &= \boldsymbol{K}_{\boldsymbol{q}} * \boldsymbol{C}_{\boldsymbol{me}}\boldsymbol{x}_{\boldsymbol{m}}\end{aligned} \tag{13}$$

$$\boldsymbol{A}_{\boldsymbol{me}} = \begin{bmatrix} \boldsymbol{0} & & \boldsymbol{I}_{\boldsymbol{n-1}} \\ -\varepsilon & -\mu - \varepsilon\tau_e \quad -g_3 \cdots - g_{n+1} & mn\tau_e^{n-1} + \mu\tau_e^n \quad -m\tau_e^n \end{bmatrix},$$

$$\boldsymbol{B}_{\boldsymbol{me}} = \begin{bmatrix} 0 \\ \vdots \\ 0 \\ 1 \end{bmatrix}_{1*n}, \quad \boldsymbol{C}_{\boldsymbol{me}} = \begin{bmatrix} \boldsymbol{C}_{\boldsymbol{me}1} \\ \vdots \\ \boldsymbol{C}_{\boldsymbol{me}N} \end{bmatrix}^{\boldsymbol{T}},$$

$$\boldsymbol{C}_{\boldsymbol{mej}} = \begin{bmatrix} 1 & C_{n-j+1}^1\tau_e & C_{n-j+1}^2\tau_e^2 & \cdots & C_{n-j+1}^{n-j+1}\tau_e^{n-j+1} & 0 & \cdots & 0 \\ 1 & C_{n-j+2}^1\tau_e & C_{n-j+2}^2\tau_e^2 & \cdots & C_{n-j+2}^{n-j+2}\tau_e^{n-j+2} & 0 & \cdots & 0 \\ \vdots & \vdots & \vdots & \ddots & \vdots & \vdots & \ddots & \vdots \\ 1 & C_n^1\tau_e & C_n^2\tau_e^2 & \cdots & C_n^{n-2}\tau_e^{n-2} & C_n^{n-1}\tau_e^{n-1} & \tau_e^n & \\ 1 & \vdots & \vdots & \ddots & \vdots & \vdots & \ddots & 0 \\ 1 & C_{n-j+N}^1\tau_e & C_{n-j+N}^2\tau_e^2 & \cdots & C_{n-j+N}^{n-j+N}\tau_e^{n-j+N} & 0 & \cdots & 0 \end{bmatrix} \tag{14}$$

g is the coefficient of combination for the dynamic characteristics of the equipment:

$$\begin{aligned} g_j &= C_n^{n-j+3}m\tau_e^{j-3} + C_n^{n-j+2}\tau_e^{j-2} + C_n^{n-j+1}\varepsilon\tau_e^{j-1}, \quad 3 \le j \le n+1 \\ n &= \frac{N(N-1)}{2}, \quad N \ge 2 \end{aligned} \tag{15}$$

$\boldsymbol{K}_{\boldsymbol{q}}$ is the steady-state operating point coefficient matrix:

$$\begin{aligned} \boldsymbol{K}_{\boldsymbol{q}} &= \boldsymbol{K}_{\boldsymbol{v}} * \overline{\boldsymbol{q}_{\boldsymbol{v}}}, \quad \overline{\boldsymbol{q}_{\boldsymbol{v}}} = \begin{bmatrix} \overline{\boldsymbol{q}_{\boldsymbol{v}(1)}} & \cdots & \overline{\boldsymbol{q}_{\boldsymbol{v}(N1)}} \\ \vdots & \ddots & \vdots \\ \overline{\boldsymbol{q}_{\boldsymbol{v}(1N)}} & \cdots & \overline{\boldsymbol{q}_{\boldsymbol{v}(N)}} \end{bmatrix} \\ \overline{\boldsymbol{q}_{\boldsymbol{v}(\boldsymbol{ij})}} &= \begin{bmatrix} \overline{q_{v(ij)}} \\ \vdots \\ \overline{q_{v(ij)}} \end{bmatrix}_{n*1}^{T}, \quad \boldsymbol{K}_{\boldsymbol{v}} = \begin{bmatrix} K_{v(1)} & \cdots & K_{v(1)} \\ \vdots & \ddots & \vdots \\ K_{v(N)} & \cdots & K_{v(N)} \end{bmatrix}_{N*(n*N)} \end{aligned} \tag{16}$$

The state-space matrices of the controlled dynamic model can be obtained as

$$\boldsymbol{A}_{\boldsymbol{m}(n*N)*(n*N)} = \boldsymbol{diag}(\boldsymbol{A}_{\boldsymbol{me}}), \quad \boldsymbol{B}_{\boldsymbol{m}(n*N)*1} = \boldsymbol{diag}(\boldsymbol{B}_{\boldsymbol{me}}), \quad \boldsymbol{C}_{\boldsymbol{m}} = \boldsymbol{K}_{\boldsymbol{q}} * \boldsymbol{C}_{\boldsymbol{me}} \tag{17}$$

The set of state vectors and the set of input and output vectors are shown below:

$$\boldsymbol{u}(k) = \begin{bmatrix} \beta_{(1)} \\ \beta_{(2)} \\ \vdots \\ \beta_{(N)} \end{bmatrix}, \quad \boldsymbol{x}_{\boldsymbol{m}}(k) = \begin{bmatrix} \boldsymbol{q}_{\boldsymbol{e}(1)} \\ \boldsymbol{q}_{\boldsymbol{e}(2)} \\ \vdots \\ \boldsymbol{q}_{\boldsymbol{e}(N)} \end{bmatrix}, \quad \boldsymbol{q}_{\boldsymbol{e}(i)} = \begin{bmatrix} q_{e(i1)} \\ q_{e(i2)} \\ \vdots \\ q_{e(ii)} \\ \vdots \\ q_{e(iN)} \end{bmatrix}, \quad \boldsymbol{y}(k) = \begin{bmatrix} q_{v(1)} \\ \vdots \\ q_{v(N)} \end{bmatrix} \tag{18}$$

where β is the corresponding flow ratio of each layer segment nozzle, q_e in $\boldsymbol{x}_{\boldsymbol{m}}$ represents the flow hysteresis change triggered by unit nozzle opening change, and the output variable q_v represents the layer segment flow. The construction of the open-loop model of the layered water injection wave code generation process has been completed.

3. **Fusion Control Algorithm.** In this section, the MPC-PID based weighted fusion control algorithm is presented. Firstly, the principle of MPC control algorithm is briefly introduced, and then the structure of MPC-PID fusion control algorithm is shown, the fusion output control law is calculated, and finally the solution steps for the optimal fusion weights are given.

3.1. **Multivariate model predictive control.** This section introduces the principles of the multivariate model predictive control algorithm. The predictive controller consists of three internal components: a known iterative model, finite time-domain optimization, and error feedback correction. A centralized parameter approach is used to control the multivariate model, and the multi-loop modified model response matrix is first loaded into the controller in the following form:

$$\boldsymbol{A}=\begin{bmatrix} \boldsymbol{A}_{11} & \cdots & \boldsymbol{A}_{1,mimo_i} \\ \vdots & \ddots & \vdots \\ \boldsymbol{A}_{mimo_o,1} & \cdots & \boldsymbol{A}_{mimo_o,mimo_i} \end{bmatrix}, \quad \boldsymbol{A_{ij}}=\begin{bmatrix} a_{ij(1)} & 0 & 0 \\ a_{ij(2)} & a_{ij(1)} & 0 \\ \vdots & \ddots & \vdots \\ a_{ij(p)} & \cdots & a_{ij(p-m+1)} \end{bmatrix} \tag{19}$$

$a_{ij(n)}$ is the nth step discrete response of the jth input corresponding to the ith output. p and m are the prediction step and control step, respectively. Input multivariate reference trajectory matrix $\boldsymbol{R_w}(\boldsymbol{k})$ as the setpoint for each loop and the real-time control output is optimal using the minimization cost function as follows:

$$\Delta \boldsymbol{u}^*(k)=\boldsymbol{L^T}\left(\boldsymbol{A^T Q A}+\boldsymbol{R}\right)^{-1}\boldsymbol{A^T Q}\left[\boldsymbol{R_w}(k)-\boldsymbol{y_{\tilde{N}0}}(k)\right] \tag{20}$$

where $\boldsymbol{L^T}$ is obtained by expanding the unit array, representing the first term of the optimal control output matrix taken. $\boldsymbol{Q}$ is the error weight matrix and $\boldsymbol{R}$ is the control weight matrix, the error vector values for each step of the same loop are selected to have the same factors of the following form:

$$\boldsymbol{Q}=\begin{bmatrix} Q_1 & \cdots & 0 & & & & \\ \vdots & \ddots & \vdots & \cdots & & \boldsymbol{0} & \\ 0 & \cdots & Q_1 & & & & \\ & \vdots & & \ddots & & \vdots & \\ & & & & Q_{mimo_o} & \cdots & 0 \\ & \boldsymbol{0} & & \cdots & \vdots & \ddots & \vdots \\ & & & & 0 & \cdots & Q_{mimo_o} \end{bmatrix}$$

$$\boldsymbol{R}=\begin{bmatrix} R_1 & \cdots & 0 & & & & \\ \vdots & \ddots & \vdots & \cdots & & \boldsymbol{0} & \\ 0 & \cdots & R_1 & & & & \\ & \vdots & & \ddots & & \vdots & \\ & & & & R_{mimo_i} & \cdots & 0 \\ & \boldsymbol{0} & & \cdots & \vdots & \ddots & \vdots \\ & & & & 0 & \cdots & R_{mimo_i} \end{bmatrix} \tag{21}$$

$mimo_i$ represents the number of input variables and $mimo_o$ represents the number of output variables. From the model structure, it is obtained that

$$mimo_i = mimo_o = N \tag{22}$$

Finally, the correction values are shifted to obtain the first prediction matrix for step $k+1$:

$$\boldsymbol{y}_{\tilde{\boldsymbol{N}}\boldsymbol{0}}(k+1)=\boldsymbol{S}\left[\boldsymbol{y}_{\tilde{\boldsymbol{N}}\boldsymbol{0}}(k)+\boldsymbol{a}_{\boldsymbol{N}}\Delta\boldsymbol{u}^{*}(k)+\boldsymbol{H}\boldsymbol{e}(k+1)\right] \tag{23}$$

where $\boldsymbol{H}$ is the feedback matrix, where the coefficients of the non-first step parameters in the feedback matrix of the same loop are set uniformly as follows:

$$\boldsymbol{H}=\begin{bmatrix} \boldsymbol{h}_1 & \cdots & 0 \\ \vdots & \ddots & \vdots \\ 0 & \cdots & \boldsymbol{h}_{mimo_o} \end{bmatrix},\quad \boldsymbol{h_t}=\begin{bmatrix} 1 \\ h_t \\ h_t \\ \vdots \\ h_t \end{bmatrix} \tag{24}$$

$\boldsymbol{e}(k+1)$ is the error vector obtained from the difference between the predicted output value and the actual value, and the displacement matrix $\boldsymbol{S}$ is a diagonal array formed by $mimo_o$ displacement matrices, and each displacement matrix element value satisfies $\boldsymbol{S_{i,i+1}}=\boldsymbol{S_{N,N}}=1$. From the solution process of the output rate, it can be seen that the parameter adjustment of one control loop of MPC will not affect the control effect of other loops, so it has certain internal decoupling ability.

3.2. **Output fusion control method.** The concrete fusion control algorithm is described in this chapter. The discrete PID controller is placed in the inner loop of the system, and the MPC controller provides the master setpoint. Since the PID algorithm is less effective in controlling the coupled system, a decoupler needs to be added to the inner loop. The multivariate coupled model is processed using a dynamic decoupling algorithm, which gives the input transformation array $\boldsymbol{M}$ and the state feedback matrix $\boldsymbol{K}$ of the decoupled system based on the state-space model.

$$\boldsymbol{K}=\boldsymbol{M}\tilde{\boldsymbol{K}}\boldsymbol{T}+\boldsymbol{M}\boldsymbol{F},\quad \boldsymbol{M}=\begin{bmatrix} \boldsymbol{C_{m1j}}\boldsymbol{A_m}\boldsymbol{B_m} \\ \boldsymbol{C_{m2j}}\boldsymbol{A_m}\boldsymbol{B_m} \\ \vdots \\ \boldsymbol{C_{mNj}}\boldsymbol{A_m}\boldsymbol{B_m} \end{bmatrix}^{-1},\quad \boldsymbol{F}=\begin{bmatrix} \boldsymbol{C_{m1j}}\boldsymbol{A_m^{mimo_o}} \\ \boldsymbol{C_{m2j}}\boldsymbol{A_m^{mimo_o}} \\ \vdots \\ \boldsymbol{C_{mNj}}\boldsymbol{A_m^{mimo_o}} \end{bmatrix}^{-1} \tag{25}$$

$\boldsymbol{T}$ in the above equation is the decoupled canonical transformation matrix, which satisfies the conditions as follows:

$$\boldsymbol{T}^{-1}(\boldsymbol{A}-\boldsymbol{B}\boldsymbol{M}\boldsymbol{F})\boldsymbol{T}=\boldsymbol{A}^{*},\quad \boldsymbol{T}^{-1}\boldsymbol{B}\boldsymbol{M}=\boldsymbol{B}^{*},\quad \boldsymbol{C}\boldsymbol{T}=\boldsymbol{C}^{*} \tag{26}$$

$\tilde{\boldsymbol{K}}$ is the pole configuration matrix, which is typically set in the negative half-plane to ensure the stability of the system. The state-space model matrix after the coupling action disappears is shown as follows:

$$\boldsymbol{A}^{\wedge}=\boldsymbol{A_m}-\boldsymbol{B_m}\boldsymbol{K},\quad \boldsymbol{B}^{\wedge}=\boldsymbol{M}\boldsymbol{B_m},\quad \boldsymbol{C}^{\wedge}=\boldsymbol{C_m} \tag{27}$$

Set the cascade partial weight coefficient array to be $\boldsymbol{w}$. Since MPC control does not require decoupling, its output is applied directly to the object and given the weight coefficient $\boldsymbol{w}'$. The algebraic relations existing between the weight matrices can be obtained as

$$\boldsymbol{w}+\boldsymbol{w}'=\boldsymbol{I}_{mimo_o*1} \tag{28}$$

Therefore, the fusion controller consists of a PID controller, an assignment session, and a centralized MPC controller, and the control output can be expressed as

$$\boldsymbol{u}=\boldsymbol{w}\boldsymbol{u_c}+\boldsymbol{w}'\boldsymbol{u_m}=\boldsymbol{w_1}\boldsymbol{u_c}+\left(\boldsymbol{I}_{mimo_o*1}-\boldsymbol{w}\right)\boldsymbol{u_m} \tag{29}$$

The controller consists of three parts. First, the MPC controller is responsible for providing the reference value for prediction optimization under the optimal index, and decoupling the influence of single-loop parameter changes on other loops, so as to achieve

independent optimization of wave code control for each layer segment. Then, the PID decoupling control link is designed to form a tandem control with MPC. The simple structure of PID control is fast, which weakens the disadvantage of slow MPC operation in complex models and improves the wave code generation speed while suppressing the sudden disturbances in the downhole transmission environment. Finally, appropriate weights are set to combine the advantages of both algorithms, which will improve the reliability of wave-code communication by improving the system response characteristics under abnormal operating conditions. The topological model of the multivariate fusion controller and the schematic diagram of the fusion control are shown in Figure 4 and Figure 5, respectively, and the above integration process can be shown as follows.

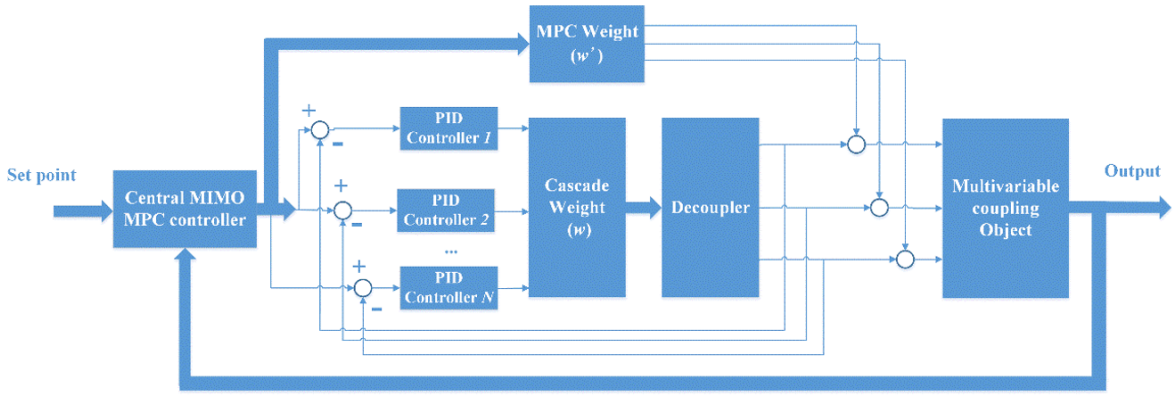

FIGURE 4. MPC-PID based multivariable fusion controller structure

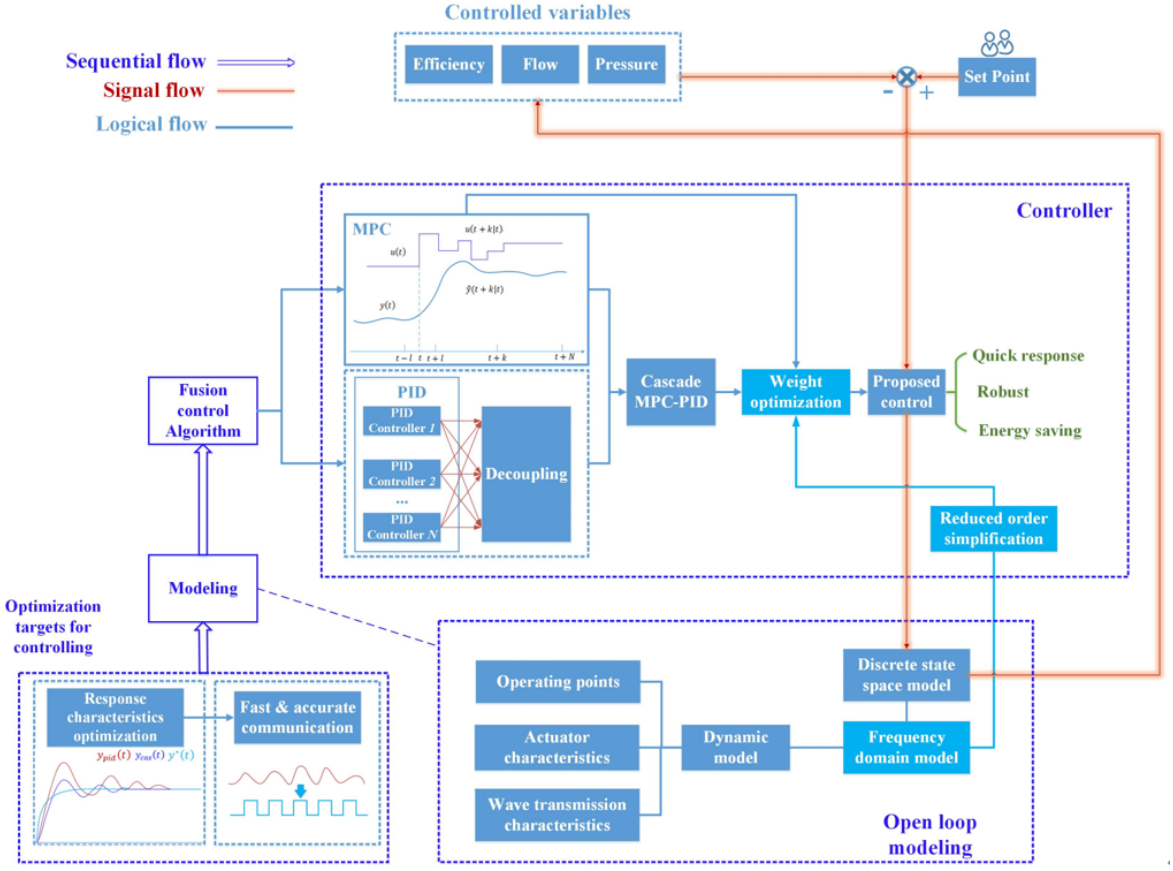

FIGURE 5. Schematic diagram of the fusion control design process

TABLE 2. The definitions of each symbol in the schematic diagram

Parameter	Description
$\boldsymbol{y_{pid}(t)}$	PID response
$\boldsymbol{y_{cas}(t)}$	Cascade MPC-PID response
$\boldsymbol{y^*(t)}$	Proposed algorithm response
$\boldsymbol{y(t)}$	Actual output
$\boldsymbol{u(t)}$	Control output
$\boldsymbol{\hat{y}(t+k|t)}$	Predicted model output after $\boldsymbol{k}$ steps
$\boldsymbol{u(t+k|t)}$	Predicted control output after $\boldsymbol{k}$ steps

Since the output of the PID control algorithm is not dependent on the model, it can be equated to an independent model with multiple parallel connections and as part of the generalized controlled system. The associated state variables of the PID controller matrix are denoted as $[A_p, B_p, \ldots]$. The target output of the generalized system can be obtained from the linear operation property of the state-space system as follows:

$$\dot{\boldsymbol{x}}_{\boldsymbol{0}} = \boldsymbol{A}\boldsymbol{X}_{\boldsymbol{0}} + \boldsymbol{B}\boldsymbol{u}, \quad \boldsymbol{y}_{\boldsymbol{0}} = \boldsymbol{C}\boldsymbol{x}_{\boldsymbol{0}} + \boldsymbol{D}\boldsymbol{u} \tag{30}$$

The generalized system is divided into two parts by the basic assignment calculation, and the corresponding weights of each part correspond to the weights of the control algorithm. According to the above analysis, the state-space model of the generalized system under MPC control can be derived as follows:

$$\begin{gathered}\boldsymbol{A} = \begin{bmatrix} \boldsymbol{A_p} & -\boldsymbol{B_p C_m w} & \boldsymbol{0} \\ \boldsymbol{B_m M C_p} & \boldsymbol{A_m - B_m K - B_m M D_p C_m w} & \boldsymbol{0} \\ \boldsymbol{0} & -\boldsymbol{B_m C_m w} & \boldsymbol{A_m} \end{bmatrix}, \quad \boldsymbol{B} = \begin{bmatrix} \boldsymbol{B_p} \\ \boldsymbol{B_m M D_p} \\ \boldsymbol{B_m} \end{bmatrix} \\ \boldsymbol{C} = \begin{bmatrix} \boldsymbol{0} & \boldsymbol{C_m w} & \boldsymbol{C_m}\left(\boldsymbol{I}_{mimo_o * 1} - \boldsymbol{w}\right) \end{bmatrix}, \quad \boldsymbol{D} = \boldsymbol{0} \end{gathered} \tag{31}$$

where the set of state and control vectors are shown as follows:

$$\begin{gathered}\boldsymbol{x_0} = \begin{bmatrix} \boldsymbol{x_{po}} \\ \boldsymbol{x_{mo}} \\ \boldsymbol{x_{co}} \end{bmatrix}, \quad \boldsymbol{x_l} = \begin{bmatrix} x_{l(1)} \\ \vdots \\ x_{l(n*N)} \end{bmatrix}, \quad \{l = po, mo, \ldots\}, \\ \boldsymbol{u} = \begin{bmatrix} \beta_{(1)} \\ \vdots \\ \beta_{(N)} \end{bmatrix}, \quad \boldsymbol{y} = \begin{bmatrix} q_{v(1)} \\ \vdots \\ q_{v(N)} \end{bmatrix} \end{gathered} \tag{32}$$

As shown by the generalized system structure analysis, $\boldsymbol{x_{po}}$, $\boldsymbol{x_{mo}}$, $\boldsymbol{x_{co}}$ correspond to the outputs $\boldsymbol{y_{po}}$, $\boldsymbol{y_{mo}}$, $\boldsymbol{y_{co}}$ of the PID controller, the cascaded weighting part of the system, and the MPC weighting part of the system, separately.

$$\boldsymbol{y_{po}} = \boldsymbol{C_p x_{po}} + \boldsymbol{D_p u}, \quad \boldsymbol{y_{mo}} = \boldsymbol{C_m x_{mo}}, \quad \boldsymbol{y_{co}} = \boldsymbol{C_m x_{co}} \tag{33}$$

Then derive the optimal fusion output controller based on the above state-space model. Firstly, the system is discretized with a sampling period of t_e, which can be obtained:

$$\begin{aligned} \boldsymbol{x_0}(k+1) &= \boldsymbol{A_0 x_0}(k) + \boldsymbol{B_0 u}(k), \\ \boldsymbol{y_0}(k) &= \boldsymbol{C_0 x_0}(k) + \boldsymbol{D_0 u}(k) \end{aligned} \tag{34}$$

The discrete system state vector after predicting N_p steps at step 0 of the controller is as follows:

$$\widetilde{\boldsymbol{x_1}}(N_p|0) = \boldsymbol{\mathcal{A}_0 x}(0) + \boldsymbol{\varphi}\Delta\boldsymbol{u}(0) \tag{35}$$

where $\boldsymbol{\mathcal{A}_0}$, $\boldsymbol{\varphi}$ are iterative state transfer vector arrays of the following form:

$$\boldsymbol{\mathcal{A}_0} = \begin{bmatrix} \boldsymbol{A_0} \\ \boldsymbol{A_0^2} \\ \vdots \\ \boldsymbol{A_0^{N_p}} \end{bmatrix}, \quad \boldsymbol{\varphi} = \begin{bmatrix} \boldsymbol{B_0} & \boldsymbol{0} & & \boldsymbol{0} \\ \boldsymbol{A_0 B_0} & \boldsymbol{B_0} & \cdots & \boldsymbol{0} \\ \boldsymbol{A_0^2 B_0} & \boldsymbol{A_0 B_0} & & \boldsymbol{0} \\ \vdots & \vdots & \ddots & \vdots \\ \boldsymbol{A_0^{N_p-1} B_0} & \boldsymbol{A_0^{N_p-2} B_0} & \cdots & \boldsymbol{A_0^{N_p-N_m} B_0} \end{bmatrix} \tag{36}$$

The predicted output of the zero-step according to the state-space model can be obtained as

$$\begin{aligned} \widetilde{\boldsymbol{y_1}}(N_p|0) &= \widetilde{\boldsymbol{y_0}}(N_p|0) + \boldsymbol{C_0}\widetilde{\boldsymbol{x_1}}(N_p|0) + \boldsymbol{D_0}\Delta\boldsymbol{u}(0) \\ &= \widetilde{\boldsymbol{y_0}}(N_p|0) + \boldsymbol{C_0}\boldsymbol{\mathcal{A}_0}\boldsymbol{x}(0) + (\boldsymbol{C_0}\boldsymbol{\varphi} + \boldsymbol{D_0})\Delta\boldsymbol{u}(0), \quad \widetilde{\boldsymbol{y_0}}(N_p|0) = \boldsymbol{0} \end{aligned} \tag{37}$$

Take the error cost function matrix of the following form:

$$\begin{aligned} \boldsymbol{J} = &\left\| \begin{bmatrix} \left[\boldsymbol{R_{w(1)}}(N_p) - \widetilde{\boldsymbol{y_{1(1)}}}(N_p|0)\right]^T \\ \left[\boldsymbol{R_{w(2)}}(N_p) - \widetilde{\boldsymbol{y_{1(2)}}}(N_p|0)\right]^T \\ \vdots \\ \left[\boldsymbol{R_{w(N)}}(N_p) - \widetilde{\boldsymbol{y_{1(N)}}}(N_p|0)\right]^T \end{bmatrix} \boldsymbol{Q} \begin{bmatrix} \boldsymbol{R_{w(1)}}(N_p) - \widetilde{\boldsymbol{y_{1(1)}}}(N_p|0) \\ \boldsymbol{R_{w(2)}}(N_p) - \widetilde{\boldsymbol{y_{1(2)}}}(N_p|0) \\ \vdots \\ \boldsymbol{R_{w(N)}}(N_p) - \widetilde{\boldsymbol{y_{1(N)}}}(N_p|0) \end{bmatrix} \right\| \\ &+ \left|\Delta\boldsymbol{u_M^T}\boldsymbol{R}\Delta\boldsymbol{u_M}\right| \end{aligned} \tag{38}$$

After minimizing the cost function, the optimal predictive control increment can be obtained as

$$\begin{aligned} \Delta\boldsymbol{u_M} = &\boldsymbol{L^T}\left[(\boldsymbol{C_0}\boldsymbol{\varphi} + \boldsymbol{D_0})^{\boldsymbol{T}}\boldsymbol{Q}(\boldsymbol{C_0}\boldsymbol{\varphi} + \boldsymbol{D_0}) + \boldsymbol{R}\right]^{-1}(\boldsymbol{C_0}\boldsymbol{\varphi} + \boldsymbol{D_0})^{\boldsymbol{T}}\boldsymbol{Q}[\boldsymbol{R_w}(N_p) \\ &- \boldsymbol{C_0}\boldsymbol{\mathcal{A}_0}\boldsymbol{x}(0)] \end{aligned} \tag{39}$$

Further, the discrete control law for the fusion controller with fixed weights is solved as

$$\begin{aligned} \boldsymbol{u}^*(z) = &\left[\left(1 - z^{-1}\right)^{-1}\Delta\boldsymbol{u_M}\right]\left\{\boldsymbol{I} + \boldsymbol{w}\left[\boldsymbol{C_p}\left(z\boldsymbol{I} - \boldsymbol{e}^{\boldsymbol{A_p}t_e}\right)^{-1}\sum_{k=0}^{\infty}[(k+1)!]^{-1}\boldsymbol{A_p^k}t_e^{k+1}\boldsymbol{B_p}\right.\right. \\ &\left.\left. + \boldsymbol{D_p} - \boldsymbol{I}\right]\right\} \end{aligned} \tag{40}$$

The real output $\boldsymbol{y_1}$ obtained from the control law input yields the following vector matrix of first-step predicted values for the next step.

$$\widetilde{\boldsymbol{y_0}}(N_p + 1|1) = \boldsymbol{S}\left[\widetilde{\boldsymbol{y_1}}(N_p|0) + \boldsymbol{H}(\boldsymbol{y_1}(N_p|0) - \widetilde{\boldsymbol{y_1}}(N_p|0))\right] \tag{41}$$

Replacing the first predicted value obtained by the loop into Equation (37) completes the cyclic prediction output of the fusion control.

3.3. **Optimal configuration of weights.** The above theory derives the algorithm principle of output fusion control, it is seen that the controller structure is more complex and the role of weights on the overall closed-loop system is uncertain. To study the fusion mechanism of MPC and PID control algorithm in depth and dissect the performance state of wave code dynamic response under the change of weights, it is necessary to study the resolution method of optimal weights of fusion control.

The analysis of the internal model structure of the fusion control is first performed. The transformation of the internal model structure aims to describe the system characteristics using a generalized frequency domain transfer function, which in turn visualizes the quantitative relationship between the weights and the output.

To obtain the internal mode structure parameters, the model structure after fusion needs to be specified. According to the first prediction link of the fusion controller, it can be derived that

$$\widetilde{\boldsymbol{y_0}}(N_p+1|1) = z\widetilde{\boldsymbol{y_1}}(N_p|0) = \boldsymbol{S}\left[\widetilde{\boldsymbol{y_1}}(N_p|0) + \boldsymbol{\varphi}\Delta\boldsymbol{u_M}(z) + z\boldsymbol{H}\boldsymbol{e}(z)\right] \tag{42}$$

A feedback error structure of the following form can also be derived as

$$\boldsymbol{e}(z) = \boldsymbol{y}(z) - \left[\boldsymbol{L^T}\boldsymbol{\varphi} + \boldsymbol{L^T}(z\boldsymbol{I}-\boldsymbol{S})^{-1}\boldsymbol{\varphi}\right]\Delta\boldsymbol{u_M}(z) - z\boldsymbol{L^T}(z\boldsymbol{I}-\boldsymbol{S})^{-1}\boldsymbol{S}\boldsymbol{H}\boldsymbol{e}(z) \tag{43}$$

The equivalent controller $\boldsymbol{G_c}$ of the internal mode structure, the internal model $\boldsymbol{G}^{\wedge}$ and the equivalent feedback filter $\boldsymbol{G_f}$ can be obtained as

$$\begin{aligned}
\boldsymbol{G_c}(z) &= \left[1+(z-1)^{-1}\right]\left[\boldsymbol{I}+\boldsymbol{I}_{N*N}\boldsymbol{\phi}(z\boldsymbol{I}-\boldsymbol{S})^{-1}\boldsymbol{S}\boldsymbol{\varphi}\right]^{-1}\boldsymbol{\phi} \\
\boldsymbol{G}^{\wedge}(z) &= z^{-2}(z-1)\boldsymbol{L^T}\left[\boldsymbol{I}+(z\boldsymbol{I}-\boldsymbol{S})^{-1}\boldsymbol{S}\right]\boldsymbol{\varphi} \\
\boldsymbol{G_f}(z) &= z\left[\boldsymbol{I}+\boldsymbol{L^T}(z\boldsymbol{I}-\boldsymbol{S})^{-1}\boldsymbol{S}\boldsymbol{H}\right]^{-1}\boldsymbol{I}_{N*N}\boldsymbol{\phi}(z\boldsymbol{I}-\boldsymbol{S})^{-1}\boldsymbol{S}\boldsymbol{H}
\end{aligned} \tag{44}$$

where $\boldsymbol{\phi}$ is the optimization coefficient matrix:

$$\boldsymbol{\phi} = \boldsymbol{L^T}\left[(\boldsymbol{C_0}\boldsymbol{\varphi}+\boldsymbol{D_0})^{\boldsymbol{T}}\boldsymbol{Q}(\boldsymbol{C_0}\boldsymbol{\varphi}+\boldsymbol{D_0})+\boldsymbol{R}\right]^{-1}(\boldsymbol{C_0}\boldsymbol{\varphi}+\boldsymbol{D_0})^{\boldsymbol{T}}\boldsymbol{Q} \tag{45}$$

The structure of the fusion control internal mode can be obtained as shown in Figure 6.

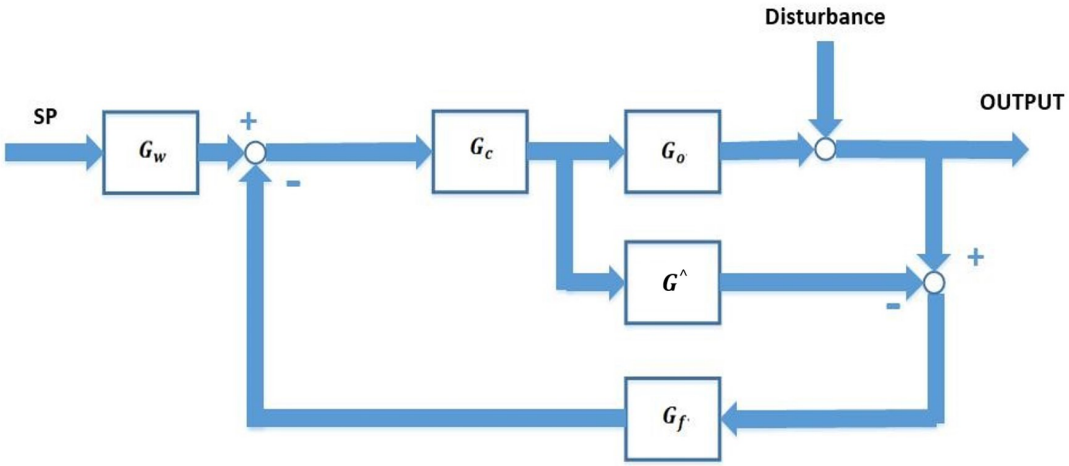

FIGURE 6. Internal mode structure of the fusion control

This leads to the total closed-loop gain of the fusion control under the internal mode structure as

$$\boldsymbol{K}(z) = \frac{\boldsymbol{G_0}(z)\boldsymbol{G_c}(z)}{\boldsymbol{I}+\boldsymbol{G_c}(z)\boldsymbol{G_f}(z)\left[\boldsymbol{G_0}(z)-\boldsymbol{G}^{\wedge}(z)\right]} \tag{46}$$

After using the final value theorem, the steady-state error expression can be derived as

$$\boldsymbol{e_{ss}} = \lim_{z\to 1}(z-1)\boldsymbol{K} = \boldsymbol{0} \tag{47}$$

Therefore, for a multivariable fusion control system with stable output, there is no steady-state residual error in the output of each loop. The above analysis shows that the total closed-loop gain model is of a high order, and to reduce the computational effort in engineering applications, it is necessary to reduce the order.

After studying the response characteristics of the system at each weight, the overall scheme of the optimal weights is given as follows: solving for the time-domain properties of the generalized model, this formula should be a function $f(t,w)$ about the weights w

and time t, and the output all peak moments are expressed as a function of the weights, so the first peak moment t_p is solved as follows:

$$T = \left\{ \frac{d(f(t,w))}{dt} = 0 \middle| \, w \right\}, \quad \left. \frac{d(f(t,w^*))}{dt} \right|_{t=t_p} = 0, \quad t_p = \min T \tag{48}$$

Since the vibration curve disappears under the optimal weight and the output reaches the set value directly after the rise, the first peak value is in the critical disappearance state, and the peak value is equal to the steady-state output value at the moment of t_s at this time, according to which it is obtained that

$$f(t_p) - f[(t_p) + N_{ps} t_e] = 0, \quad N_{ps} \in \left(\frac{t_p}{t_e}, \frac{t_s}{t_e} \right] \tag{49}$$

where N_{ps} indicates the number of steps from peak to steady-state. Based on the above theory, the following algorithm for solving the optimal weight theory solution $\boldsymbol{w}^*$ can be derived by combining the simulation curves.

1) Performing a Tustin bilinear transformation on the controller part of the internal modalized output gain $\boldsymbol{K}$, where the $\boldsymbol{G_0}$ model part can be directly replaced using the following equation:

$$\boldsymbol{G_0}(s) = \boldsymbol{C_0}(s\boldsymbol{I} - \boldsymbol{A_0})^{-1}\boldsymbol{B_0} + \boldsymbol{D_0} \tag{50}$$

$\boldsymbol{G_0}$ is the frequency domain model matrix of $mimo_o$ rows and $mimo_i$ columns, and the total output gain of $mimo_o$ terms is normalized to the following form:

$$\begin{aligned} \boldsymbol{K}(s) &= \begin{bmatrix} K_1(s) \\ \vdots \\ K_{mimo_o}(s) \end{bmatrix} \\ &= \begin{bmatrix} \left[s^p + c_{1(1)}s^{p-1} + \cdots + c_{p(1)}\right]^{-1} \left[d_{1(1)}s^{p-1} + \cdots + d_{p(1)}\right] \\ \vdots \\ \left[s^p + c_{1(mimo_o)}s^{p-1} + \cdots + c_{p(mimo_o)}\right]^{-1} \left[d_{1(mimo_o)}s^{p-1} + \cdots + d_{p(mimo_o)}\right] \end{bmatrix} \end{aligned} \tag{51}$$

2) Use reduced-order equivalent transformation and set the downscaled order as r. The output gain of the tth term can be approximated as

$$\widetilde{\boldsymbol{K_o}}(s) = \sum_{j=1}^{r} \beta_j \prod_{i(t)=2}^{j} \left[\left(\alpha_{i(t)} s + \left(\alpha_{i(t-1)} s \right)^{-1} \right)^{-1} \right]^{(r)}, \quad r < \frac{p}{2} \tag{52}$$

where α, β are the weight correlation coefficients, which can be obtained by an iterative procedure, generally taking the calculated results after 2-3 iterations.

3) The frequency domain analysis of the reduced-order model is performed to obtain the weight-dependent output characteristics. To analyze the role played by the weights under each loop, it is necessary to categorize the discussion concerning the output characteristics: Fusion optimization should take reducing the overshoot as the primary target, and if the original string-level control output overshoot is small, the weight w should be increased appropriately to retain the good dynamic performance of the lower-level PID. Conversely, if the original cascade control output oscillation is strong or the overshoot is large, the weight w should be reduced to increase the robust performance of MPC control. Under the optimal weight, the first time the overshoot-free output curve reaches the peak is steady-state, so the difference between the steady-state time and the first peak time must be extremely small, according to which the following weight solution equation can be

derived as

$$\begin{cases} \begin{cases} w_\sigma^* = \max \mathcal{W}^*, & \sigma(w) > 0 \\ \overline{w_\sigma^*} = \min \mathcal{W}^*, & \sigma(w) = 0 \end{cases} \\ \mathcal{W}^* = \begin{cases} \arg\min \left| \pi - \dfrac{2\beta_1(w) arctg\delta(w)}{2\beta_2(w) - \alpha_1(w)\beta_1(w)} - \dfrac{[8 + 2\ln\sigma(w)]\delta(w)}{\alpha_1(w)} \right|, & \sigma(w) > 0 \\ \arg\min \left| \pi - \dfrac{2\beta_1(w) arctg\delta(w)}{2\beta_2(w) - \alpha_1(w)\beta_1(w)} - \dfrac{8\delta(w)}{\alpha_1(w)} \right|, & \sigma(w) = 0 \end{cases} \end{cases} \tag{53}$$

where δ is related to the output damping ratio of the fusion control concerning the vibration frequency, note that the system output is the first peak at the maximum overshoot, so δ takes the value in the first cycle.

$$\delta(w) = \sqrt{\alpha_2(w) - \frac{\alpha_1^2(w)}{4}}, \quad \delta(w) \in \left(-\frac{\pi}{2}, \frac{\pi}{2}\right) \tag{54}$$

σ is the overshoot discriminant function.

$$\sigma(w) = \sqrt{1 - \alpha_1(w)\frac{\beta_1(w)}{\beta_2(w)} + \alpha_2(w)\left[\frac{\beta_1(w)}{\beta_2(w)}\right]^2\Bigg|_{w=1}} \tag{55}$$

$\mathcal{W}^*$ represents the set of weight solutions without overshooting the output at the minimum difference between t_p and t_s, so satisfying the $\mathcal{W}^*$ set basis constraint is a necessary and non-sufficient condition for weight optimization. Therefore, in order to balance the optimal performance of the dual algorithm, an analysis of the optimal selection of the solution set is required: if there is overshoot in the string-level output, $*$ allows a small range of changes in the string-level weights w_σ^* at this time, and at this time, to speed up the system response, the maximum value under the $\mathcal{W}^*$ constraint should be selected. On the other hand, if the original output does not have overshoot, the value range of $\overline{w_\sigma^*}$ is expanded. To compensate for the weakened MPC robust performance, the minimum value in the set should be taken. Therefore, under the same control loop, the original cascade output has overshoot. The optimal fusion weight w_σ^* and the weight when the cascade output has no overshoot $\overline{w_\sigma^*}$ have the following relationship:

$$\mathcal{W}^* = (0, w_\sigma^*] \cup [\,\overline{w_\sigma^*}, 1)\,, \quad \overline{w_\sigma^*} > w_\sigma^* \tag{56}$$

In conclusion, the optimal system first needs to satisfy the primary performance constraint of overshoot-free output, while considering the secondary performance of response speed or robustness.

4. Simulation Results Analysis and Discussion.

4.1. Control simulation and verification. In this section, a simulation scenario of a three-variable equivalent model for layered water injection is designed to show the response characteristics in the form of intuitive curves for different control algorithms for flow, pressure and related parameters of water distribution equipment under various operating conditions. Several evaluation metrics are also selected to objectively describe and compare the performance of different algorithms. The simulation compares the PID control algorithm, MPC control algorithm, MPC-PID cascade control algorithm, and fusion control algorithm with the target. The simulation operations were performed on a machine with Intel i5 CPU with 16G running memory. Firstly, the layer segment flow control simulation is conducted, in order to simulate various sudden actual working conditions, the sudden change link of the set value is introduced, and the step jump is set to be carried out in asynchronous order to check the mutual disturbance effect of multi-loop

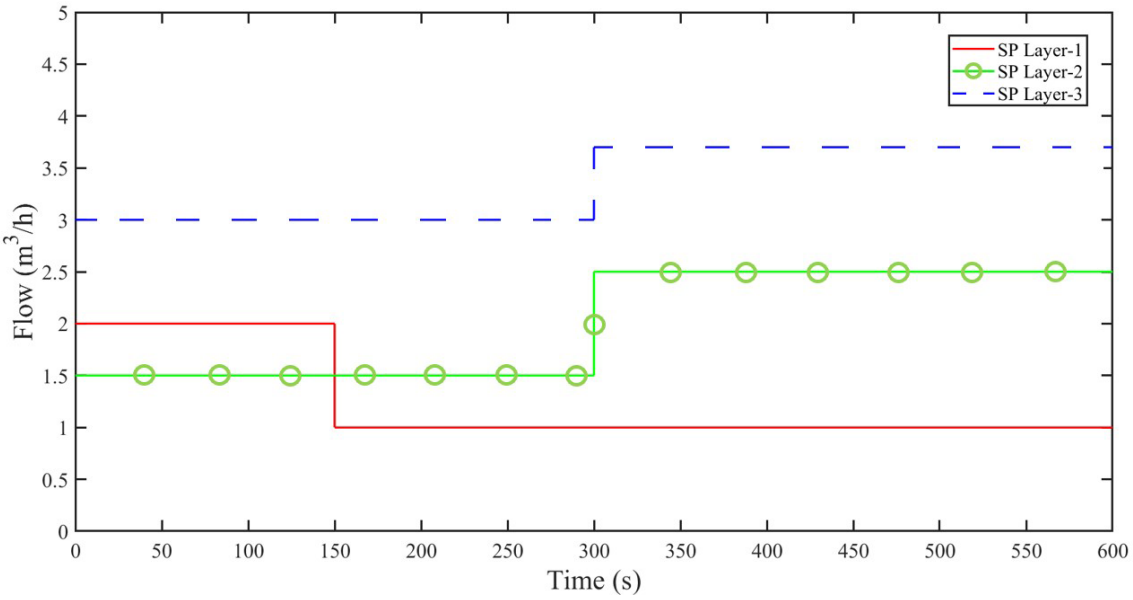

FIGURE 7. Flow value setting curves for each layer

control output change. The input setting signal curve of the control system is shown in Figure 7. The flow value of the first layer section starts at 2 m^3/h and then drops to 1 m^3/h at 150 s; the flow value of the second layer section is initially set at 1.5 m^3/h and rises to 2.5 m^3/h at 300 s; the flow value of the third layer section is initially set at 3 m^3/h and rises to 3.7 m^3/h at 300 s.

To achieve a rigorous comparison, the control variable principle is used and all control algorithms are selected with the same common parameter metrics to compare the impact of the algorithm under independent parameters on the control performance. The non-optimal MPC parameters were selected as shown in the following Table 3.

TABLE 3. Basic MIMO-MPC design parameters

Parameters	Value
Control horizon	1
Prediction horizon	25
Error weight ($[\boldsymbol{Q_1}, \boldsymbol{Q_2}, \boldsymbol{Q_3}]$)	$[0.2, 0.15, 0.5]$
Control weight ($[\boldsymbol{R_1}, \boldsymbol{R_2}, \boldsymbol{R_3}]$)	$[5.7, 2.5, 7]$
Correction coefficient ($[\boldsymbol{h_1}, \boldsymbol{h_2}, \boldsymbol{h_3}]$)	$[0.35, 0.25, 0.15]$

The dynamic performance of the flow value of each layer segment under PID and MPC-PID cascade control algorithms is illustrated in Figure 8. The output under different algorithms realizes effective tracking of the set value, while the amplitude oscillation of the cascade algorithm is significantly weakened, but the steady-state is equal to the result of the PID algorithm. When the output is disturbed at 450 s and 550 s, the output is more affected under PID control than others. The cascade algorithm uses MPC as the main controller, which has better performance than the PID control algorithm in terms of overshoot reduction and disturbance recovery, but the steady-state time is still longer and oscillation exists. The selection of the PID controller parameters is shown in the following Table 4.

Figure 9 shows the dynamic changes of the flow value in the lower layer segment for MPC, cascaded MPC-PID, and the proposed algorithms. As shown in the figure, all

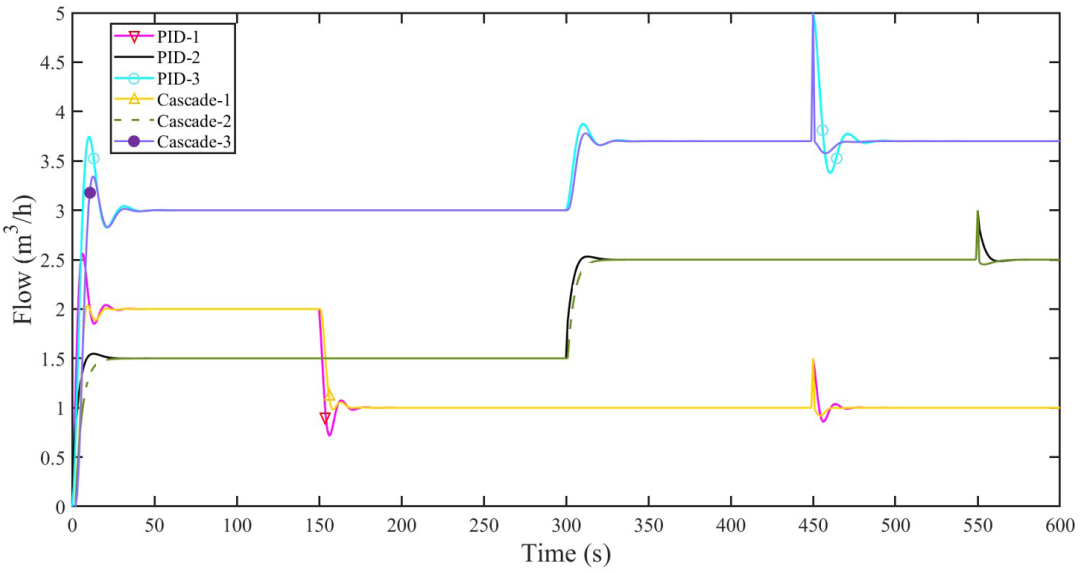

FIGURE 8. Layer flow control simulation results of PID and cascade MPC-PID

TABLE 4. PID controller common parameters

Parameters	Value
$\boldsymbol{K_p}$	$[2.75, 3.00, 7.67]$
$\boldsymbol{T_i}$	$[1.00, 0.77, 2.00]$
$\boldsymbol{T_d}$	$[0.67, 0.37, 1.33]$

control algorithms eliminate the steady-state error and achieve accurate control of the flow. It is calculated by 3.3 that the control effect of each loop is best when the weight matrix $\boldsymbol{w}$ is taken as $[0.625, 0.57, 0.25]^T$. The target algorithm maintains the response speed of the string-level control algorithm, which is significantly improved compared with the non-optimized parameter MPC algorithm. It can be seen that the target algorithm does not need to fine-tune the complex parameters of the MPC controller, but only needs to change the weights to complete the process of performance optimization, which simplifies the operation process. Compared with the cascade control algorithm, the amount of oscillation and overshoot is weakened, which is mainly due to the addition of the MPC weight control component and reasonable weight ratios, which shorten the steady-state establishment process time, track the set value faster, and improve the dynamic response performance.

To verify the dynamic performance of various algorithms comprehensively, several performance metrics were selected for comprehensive comparison, and the results are shown in Table 5, where H represents the lift of the pump, $\boldsymbol{\sigma_p}$ is the overshoot when the curve starts from 0 s and the output reaches the set value, $\boldsymbol{\sigma_d}$ is the overshoot when the output returns to steady state after a strong disturbance at 450 s, $\boldsymbol{t_s}$ is the steady state time, and $\sum \boldsymbol{L_u}$ is the cumulative change amplitude of each output control signal during the overall control process.

To test the control performance of each algorithm and the change of the working state of the equipment under the abnormal control state comprehensively, the simulation of the working condition with unstable discrete sampling frequency under the same weight was performed, and the simulation results of the pump head, full well flow, pump efficiency and the control signal curve received by the underground water distributor are shown in Figure 10.

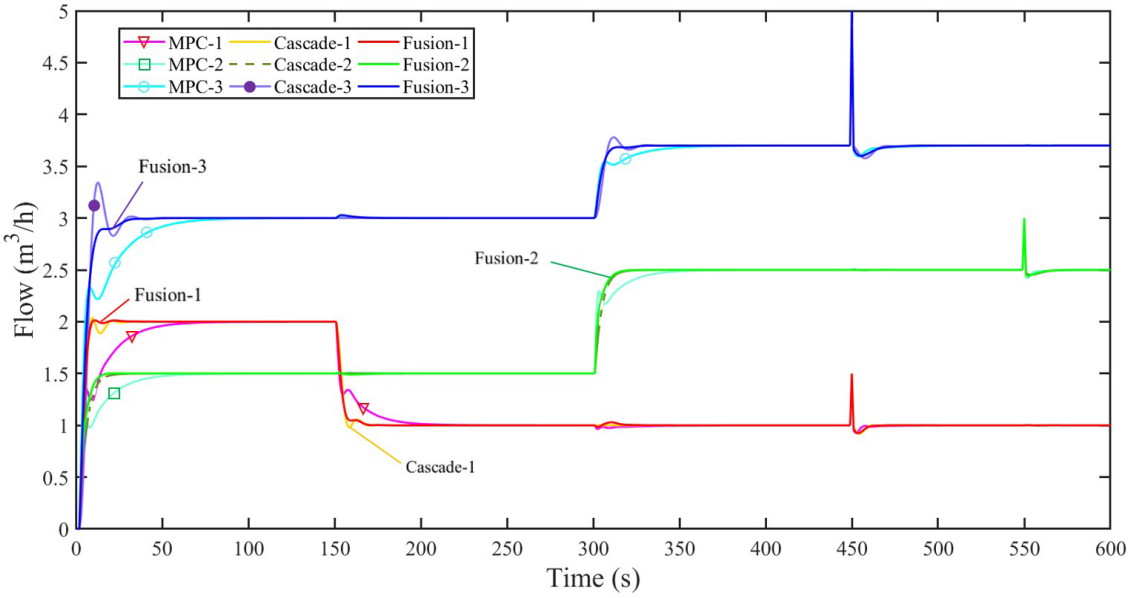

FIGURE 9. Layer flow control simulation results of PID, cascade MPC-PID, and fusion

TABLE 5. Dynamic performance index evaluation

Algorithm	$\boldsymbol{\sigma_p}$ (%)		$\boldsymbol{\sigma_d}$ (%)		$\boldsymbol{t_s}$ (s)	$\sum \boldsymbol{L_u}$
	q_v	H	q_v	H		
PID	13.65	21.49	6.45	9.23	62	5.826
MPC	0	0	2.46	6.36	99	3.826
Cascade	8.15	14.29	2.54	6.80	63	4.128
Fusion	0	0	2.42	5.81	55	2.907

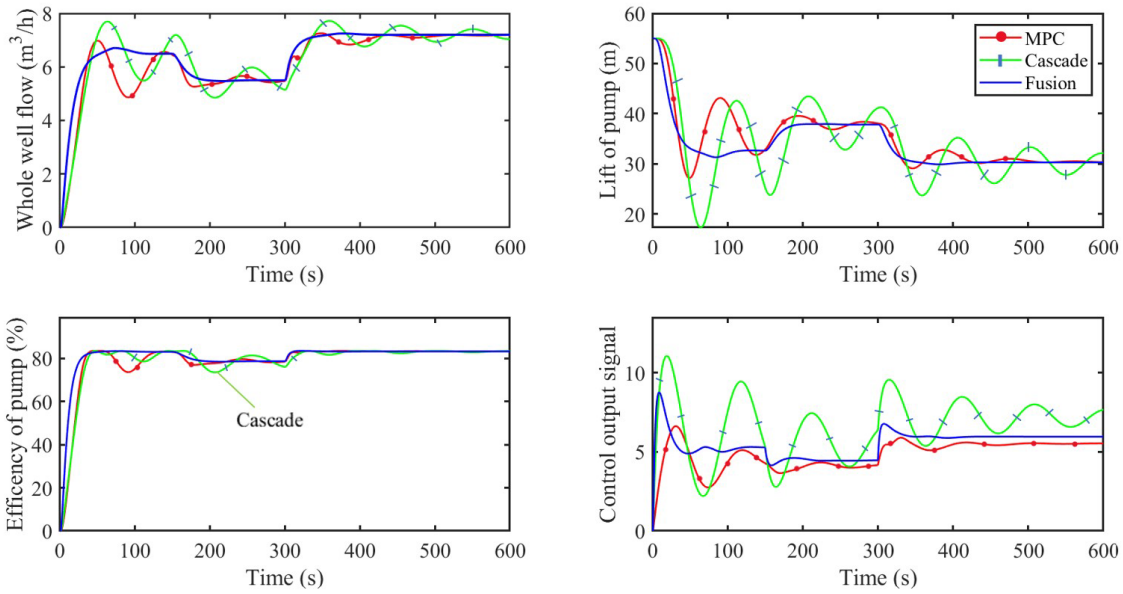

FIGURE 10. Variation of equipment operating parameters under poor sampling settings

In the state of poor sampling settings, the MPC and cascade MPC-PIC algorithm controls the whole well flow and pump efficiency fluctuations, and the pump lift oscillation amplitude is large, while the target algorithm maintains the stability of each parameter control and weaken the fluctuation of the water distributor signal. Weakening the fluctuation of full well flow will avoid the water hammer effect and protect the piping equipment. Meanwhile, maintaining the stability of efficiency will effectively extend the service life of water distribution equipment.

4.2. **Wave code communication simulation optimization.** Control algorithm optimization is mainly aimed at improving the decoding success rate of intelligent water injection communication. The quality of generation depends on the generation time of the parametric wave code and its approximation to the standard square wave. Figure 11 shows the actual generated wave codes. In the above figure, the wave code is weak and the wellhead cannot be recognized, resulting in decoding failure. Therefore, the following figure increases the amplitude of openness fluctuation, the wave code pattern is more obvious, and the decoding success rate is improved. However, since the signal curve has a larger error than the standard square wave, there is still a distortion of the decoded data, resulting in the user not being able to collect the real physical data of the well in the upload communication, while the failure of decoding or miscoding of the downhole controller in the downlink communication will lead to mis-operation of underground water distributor.

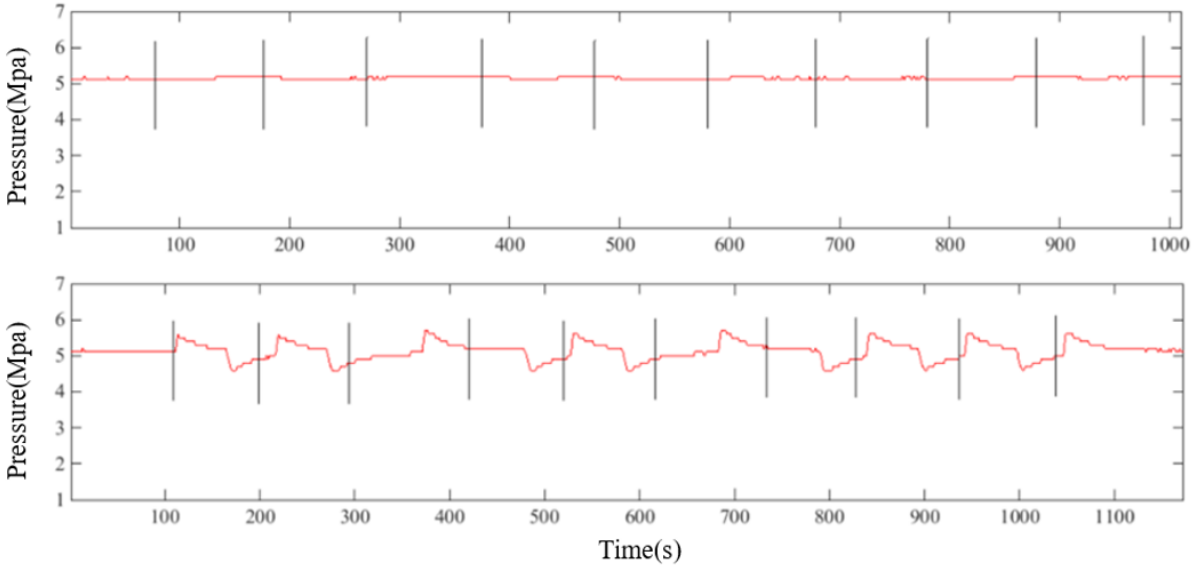

FIGURE 11. Actual communication wave code generated by fluid fluctuations

Figure 12 illustrates the simulation results of the layer segment flow wave code signal, comparing the wave code effect generated by the three control algorithms. The nozzles in the 1st and 3rd layers change periodically during the 400∼1200 s stage to generate flow wave coding, in which the layer-3 target signal is 3∼3.7 m^3/h amplitude, and the first layer target wave coding amplitude is 1∼2 m^3/h, the later period is 2∼2.5 m^3/h, and the second layer section maintains 1.5 m^3/h constant. The figure shows that the process of the curve's progressive amplitude in the MPC algorithm is slow, the tracking performance is poor, and the generated wave code has a large curvature. Cascade control algorithm has a certain amplitude of oscillation overshoot, which can destroy the wave code curve structure, resulting in lower decoding pass rate and data distortion. Since

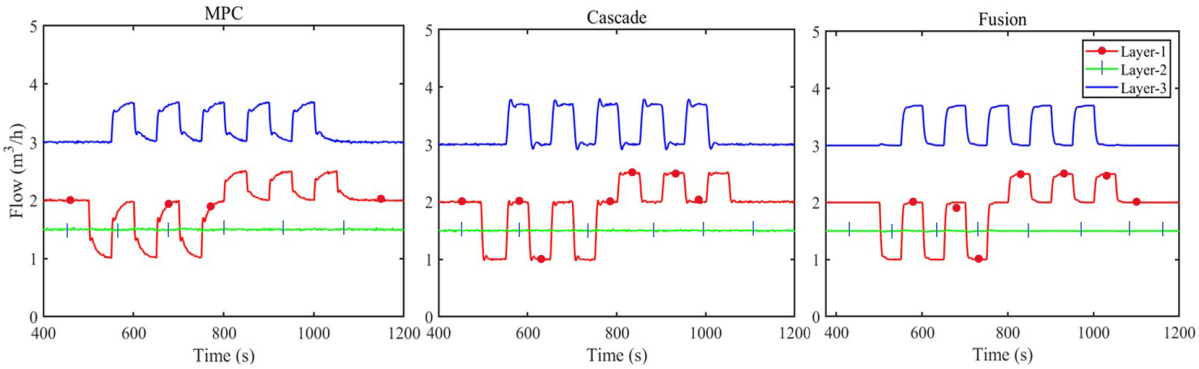

FIGURE 12. Simulation results of flow wave code signals for each layer

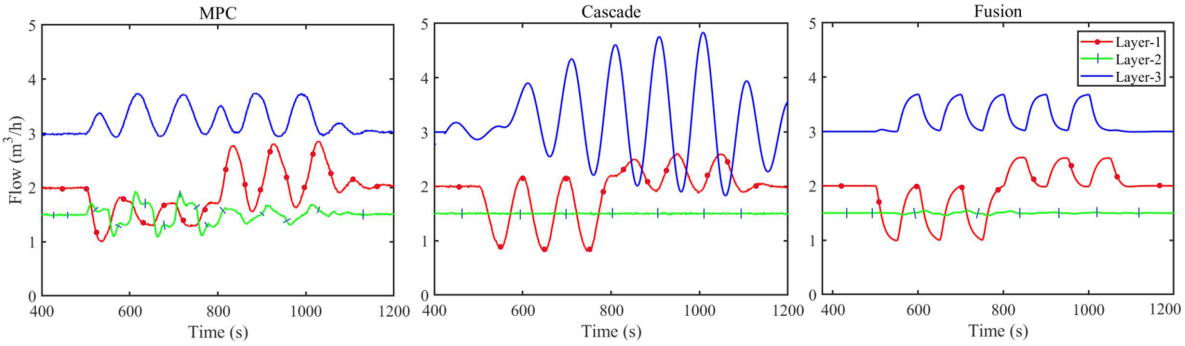

FIGURE 13. Comparative simulation results of layer segment flow wave code signal robustness

the wave code curve of the target fusion control algorithm is closest to the target square wave, it is possible to achieve fast and accurate decoding in this state even with reduced fluctuation amplitude compared to the more stringent wave code amplitude conditions in other algorithms, and to achieve the goal of power-saving by reducing the reciprocal stroke of the valve action.

For closer approximation to the actual working conditions, this paper studies the control situation when the controller load model and the actual controlled system model are severely mismatched, the system output is more unstable in this state, and the robustness of different control algorithms can be compared critically and clearly without changing the weight matrix. A comparison of the layer section flow wave code signal effects is shown in Figure 13. It can be seen that the MPC algorithm control recovery is slow, and the wave code amplitude is not fixed, which generates multiple wave peaks and is easy to cause false codes. Compared with the output steady-state of Figure 12, the defects of the cascade MPC-PID algorithm are more obvious. The amplitude of the output oscillation of the third layer segment is further increased compared with the MPC algorithm, and the error is great compared with the control results of the algorithm in Figure 13, and the controlled signal has a trend of divergence because the underlying PID algorithm amplifies the role of large model mismatch in proportional form and exacerbates the system instability by differentiation, which is more obvious when controlling the model with large steady-state gain. The proposed algorithm maintains the fast response of the rising phase, oscillations are substantially weakened, the wave code signals generated at different periods are of the same amplitude, and the output converges quickly to the original setting after wave code abort. In conclusion, the quality of the generated wave code is relatively high, which

is mainly due to the robust effect of MPC superimposed on the attenuating effect of the cascade weighting factor on the mismatch error.

For a more realistic and comprehensive simulation of the controller model mismatch conditions, robust simulations of the full well flow, pressure wave code, water distributor control signal and pumping machine efficiency were performed simultaneously with the wave code generation process. The simulation results are shown in Figure 14.

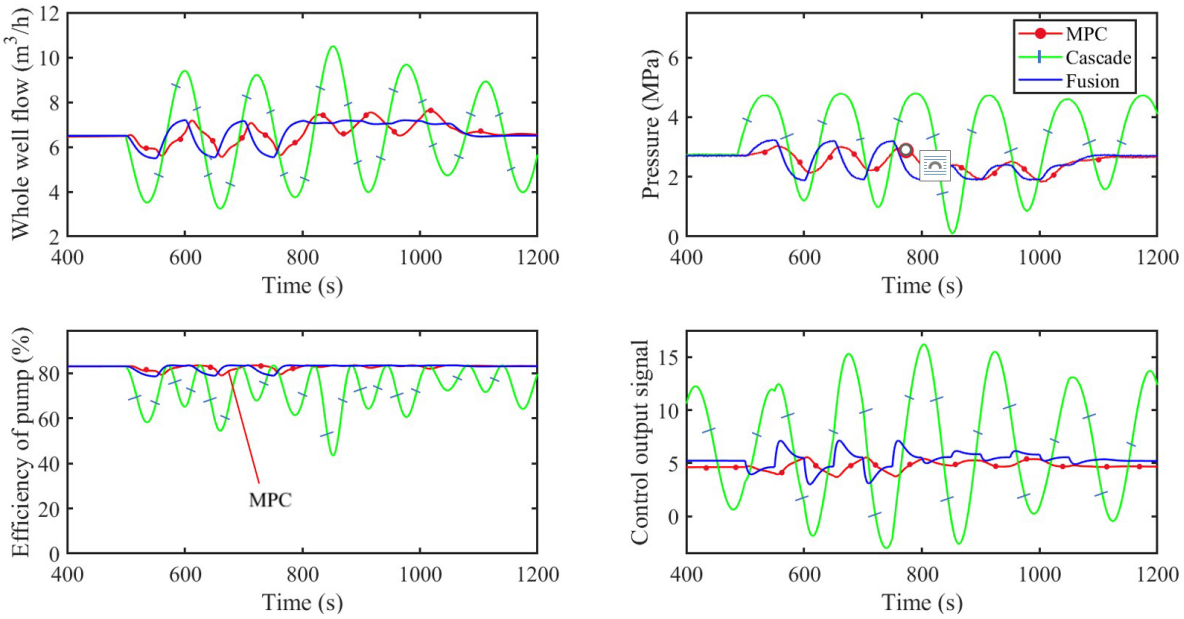

FIGURE 14. Comparative simulation results of equipment operating parameters robustness

As shown in the figure, during the wave code generation phase from 500 s to 800 s, the wave codes generated between first and third layer sections have the same direction, so the whole well flow value changes more under the control of MPC and the proposed algorithm. While the wave codes in the double layer sections have opposite directions from 800 s to 1200 s, the proposed algorithm maintains a constant whole well flow and avoids ineffective fluctuations that MPC produces, while the control performance of the string-level MPC-PID algorithm deteriorates severely throughout. Meanwhile, the pressure fluctuations under the cascade MPC-PID algorithm are more violent, which may cause the sealing device to fail, leading to uncontrolled and undifferentiated water injection in each layer. MPC algorithm generates pressure waves with irregular amplitude and large curvature of wave code signal, which is not conducive to decoding. The fusion control algorithm generates pressure waves of consistent amplitude at different periods, and the waveform is controlled within a reasonable and identifiable range, which is more compliant than other algorithms. MPC-PID cascade algorithm output control signal appears to be overloaded, the output of the negative signal will reverse the voltage, drive the water distributor nozzle repeatedly action, losing power, making energy use efficiency reduced. In the simulation of pumping machine efficiency, the efficiency of the pumping machine under MPC and the proposed algorithm is stable and maintained at about 80%, with less effect from the change of full well flow value. The pumping machine efficiency fluctuates unstably under the cascade algorithm, and the generation of wave code causes the efficiency to drop rapidly to 50%∼60%, resulting in larger power loss. While the fusion-controlled pumping machine efficiency is maintained at 800 s∼1200 s, which meets the requirements of efficient energy utilization and protection of equipment.

As mentioned above, the fusion control algorithm proposed in this paper is superior to the traditional control algorithm in terms of response speed, stability and robustness for the long-term fast fluctuation control process of large time lag, multivariate model systems. Compared with the MPC control algorithm, satisfying the good control effect allows a larger adjustment range of the controller parameters, the fusion control algorithm further shrinks the overshoot and shortens the steady-state time compared with the MPC-PID cascade control algorithm, and in the case of anomalous states where the MPC controller does not match the actual model, the role of the appropriately proportioned MPC control output enhances the system. The fusion control algorithm maximizes the use of model parameters to achieve fast and efficient control, reflecting its specialization over the fuzzy PID control algorithm, while the appropriately scaled fusion control law output ensures fast and stable following of the target set value by the system, thus achieving a good control qualification rate.

4.3. **Response characteristics analysis.** This section clarifies the mechanism of optimal fusion control by visually demonstrating the fusion effect of MPC and PID algorithms with different weights. Figure 15 records the output curves for each loop string section weight as the uniform step size increases. The output overshoot of the first loop gradually decreases until the output curve fits exactly with the set value, at this point, if the weight value is increased again, it will intensify the vibration of the system and make the steady-state time longer. If the weight in the second output continues to increase beyond the optimal value, it will not increase the overshoot, but the output curve will gradually shift downward away from the set value curve, which will slow down the steady-state establishment process. In the first and second outputs, the optimal weights are selected as the minimum value in the overshoot-free weight set, preserving the favorable performance of the lower-level PID. In the third output, the original cascade algorithm output oscillation is violent and dynamic performance is poor, so reducing the cascade control weights is necessary. The optimal output curve fits exactly with the set value, and at this point, if w continues to be reduced, it will weaken the fast response characteristics of the system. Optimal weights can be calculated from (53) to (55).

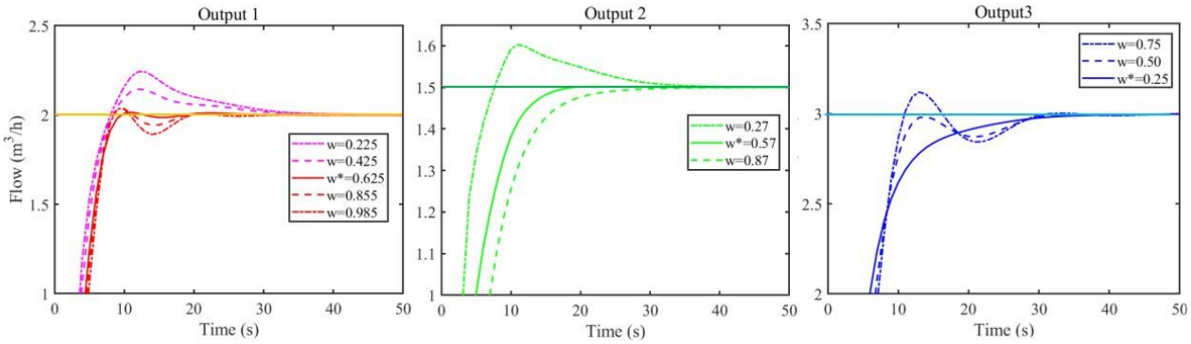

FIGURE 15. Output of different weights in different control loops

To ensure the universality of the optimal dynamic performance of the fusion control, the three output loops cover all types of output curves of the cascade control algorithm. Output 1 overshoot is much smaller, but oscillation exists. Output 2 has no overshoot and no oscillation. Output 3 overshoot and oscillation exist simultaneously. In particular, in the 3-loop, as long as the first peak of the output curve under the specified weights is guaranteed to be no greater than the set value, the overshoot is eliminated, optimizing the control performance of the large steady-state gain object, with good performance

of the lower-level PID. All in all, the optimal fusion control has accomplished the task of optimizing the dynamic performance of multivariable inertia link control under the condition that the controller parameter regulation is refined and simplified.

5. **Conclusion.** In this paper, an MPC-PID-based output optimal fusion control method is designed to effectively improve the control response characteristics of fluid wave codes, which enhances the wave code communication efficiency of oilfield layered water injection. The wave code generation model is built based on the whole-well pressure and flow characteristics. The optimal fusion control law is solved when minimizing the cost function under fixed weights, and the fusion mechanism of MPC and PID algorithms is analyzed to explore the performance state of the system output under different fusion weights, completing the theoretical solution of the optimal fusion weights. The simulation results show that the fusion control method has fast following capability, generates wave codes with high speed and high quality, and ensures the reliability of wave code data under abnormal working conditions to achieve efficient communication of oilfield water injection production data.

Acknowledgments. The authors sincerely thank the support for the Research Institute of Petroleum Exploration & Development and the help of senior brothers and sisters.

REFERENCES

[1] X. M. Song, D. B. Qu and C. Y. Zou, Low cost development strategy for oilfields in China under low oil prices, *Petroleum Exploration and Development*, vol.48, no.4, pp.1007-1018, 2021.
[2] H. B. Li, Z. M. Yang, R. S. Li et al., Mechanism of CO_2 enhanced oil recovery in shale reservoirs, *Petroleum Science*, vol.18, no.6, pp.1788-1796, 2021.
[3] T. Liang, J. R. Hou, M. Qu et al., Application of nanomaterial for enhanced oil recovery, *Petroleum Science*, vol.19, no.2, pp.882-899, 2022.
[4] A. Mohamed, Z. Y. Wu and D. Y. Zhou, A review of chemical-assisted minimum miscibility pressure reduction in CO_2 injection for enhanced oil recovery, *Petroleum*, vol.7, pp.245-253, 2021.
[5] E. Ajoma, S. Saira, T. Sungkachart et al., Water-saturated CO_2 injection to improve oil recovery and CO_2 storage, *Applied Energy*, vol.226, DOI: 10.1016/j.apenergy.2020.114853, 2020.
[6] J. Jiang, Z. Rui, R. Hazlett and J. Lu, An integrated technical-economic model for evaluating CO_2 enhanced oil recovery development, *Applied Energy*, vol.247, pp.190-211, 2019.
[7] X. Wang, V. Klaasvan, P. Marcy et al., Economic co-optimization of oil recovery and CO_2 sequestration, *Applied Energy*, vol.222, pp.132-147, 2018.
[8] P. Luo, W. G. Luo and S. Li, Effectiveness of miscible and immiscible gas flooding in recovering tight oil from Bakken reservoirs in Saskatchewan, Canada, *Fuel*, vol.208, pp.626-636, 2017.
[9] D. L. Guo, Y. W. Kang, Z. Y. Wang et al., Optimization of fracturing parameters for tight oil production based on genetic algorithm, *Petroleum*, vol.8, no.2, pp.252-263, 2022.
[10] X. L. Wang, P. C. Wu, Y. P. Han et al., Current situation and measures of water injection in Chang 8 Layer, Xifeng Oilfield, Changqing Oilfield, *Petroleum Exploration and Development*, vol.35, no.3, pp.344-348, 2008.
[11] W. B. Zhao, S. Y. Hu and X. Q. Deng, Physical property and hydrocarbon enrichment characteristics of tight oil reservoir in Chang 7 division of Yanchang Formation, Xin'anbian oilfield, Ordos Basin, China, *Petroleum Science*, vol.18, no.5, pp.1294-1304, 2021.
[12] N. W. Zhou, S. F. Lu, M. Wang et al., Limits and grading evaluation criteria of tight oil reservoirs in typical continental basins of China, *Petroleum Exploration and Development*, vol.48, no.5, pp.1089-1100, 2021.
[13] T. A. Ganat, M. Hrairi, M. Farj et al., Development of a novel method to estimate fluid flow rate in oil wells using electrical submersible pump, *Journal of Petroleum Science and Engineering*, vol.135, pp.466-475, 2015.
[14] G. L. Jing, S. Tang, X. X. Li and H. Y. Wang, The analysis of scaling mechanism for water injection pipe columns in the Daqing Oilfield, *Arabian Journal of Chemistry*, vol.10, pp.1235-1239, 2017.

[15] L. M. Zhang, C. Xu, K. Zhang et al., Production optimization for alternated separate-layer water injection in complex fault reservoirs, *Journal of Petroleum Science and Engineering*, vol.193, DOI: 10.1016/j.petrol.2020.107409, 2020.
[16] D. L. Jia, H. Liu, J. Q. Zhang et al., Data-driven optimization for fine water injection in a mature oil field, *Petroleum Exploration and Development*, vol.47, no.3, pp.674-682, 2020.
[17] Y. P. Zhou, Research and application of preset cable intelligent injection technology, *Oil Field Equipment*, vol.48, no.4, pp.69-73, 2019 (in Chinese).
[18] Z. L. Li, Development status and application prospect of intelligent separation injection technology, *New Material and New Technology*, vol.45, no.7, 2019 (in Chinese).
[19] Y. Tong, Wireless remote intelligent water injection control system discussion, *Chemical Engineering & Equipment*, vol.7, 163000, 2020 (in Chinese).
[20] B. Yao, L. Z. Yang and J. Z. Yu, Digital layered water injection based on wave code communication, *J. China Petroleum Machinery*, vol.48, no.5, pp.71-77, 2020 (in Chinese).
[21] X. Qian, S. K. Jia, K. J. Huang et al., MPC-PI cascade control for the Kaibel dividing wall column integrated with data-driven soft sensor model, *Chemical Engineering Science*, vol.231, DOI: 10.1016/j.ces.2020.116240, 2021.
[22] S. Ravendra, I. Marianthi and R. Rohit, System-wide hybrid MPC-PID control of a continuous pharmaceutical tablet manufacturing process via direct compaction, *European Journal of Pharmaceutics and Biopharmaceutics*, vol.85, pp.1164-1182, 2013.
[23] S. Ravendra, S. Abhishek, M. Krizia et al., Implementation of an advanced hybrid MPC-PID control system using PAT tools into a direct compaction continuous pharmaceutical tablet manufacturing pilot plant, *International Journal of Pharmaceutics*, vol.473, pp.38-54, 2014.
[24] Y. M. Ni, Fusion control strategy based on I-Fuzzy-Smith algorithm for complex process with large lag, *Hydro Mechatronics Engineering*, vol.41, no.18, 2013.
[25] G. Chen, S. Lv and J. Dai, Study on PID control of vehicle semi-active suspension based on genetic algorithm, *International Journal of Innovative Computing, Information and Control*, vol.15, no.3, pp.1093-1114, 2019.
[26] M. Zhuang and Q. Zhu, The internal mode fractional-order PID control based on neural network for the temperature of air-conditioned rooms, *International Journal of Innovative Computing, Information and Control*, vol.17, no.3, pp.1019-1028, 2021.
[27] R. Kurokawa, N. Kawaguchi, T. Sato and R. Vilanova, Data-driven regulator PID control using a model-reference robust tuning method, *International Journal of Innovative Computing, Information and Control*, vol.18, no.1, pp.1-13, 2022.
[28] Z. H. Deng, Q. H. Chen, L. Y. Zhang et al., Weighted fusion control for proton exchange membrane fuel cell system, *International Journal of Hydrogen Energy*, vol.45, pp.15327-15355, 2020.
[29] J. Severiano, A. Silva, A. Sussush et al., Corrosion damages off low regulation valves for water injection in oilfields, *Engineering Failure Analysis*, vol.96, pp.362-373, 2019.
[30] S. S. Gao, Y. Yi and G. Z. Liao, Experimental research on inter-fracture asynchronous injection-production cycle for a horizontal well in a tight oil reservoir, *Journal of Petroleum Science and Engineering*, vol.208, 109647, 2022.
[31] X. Zhang, S. L. Yang, B. Wen et al., Experimental study on threshold pressure gradient of CO_2 miscible flooding in low permeability reservoir, *Petroleum Geology & Experiment*, vol.35, no.5, pp.583-586, 2013.
[32] W. Xiong, Q. Lei, X. G. Liu et al., Pseudo threshold pressure gradient to flow for low permeability reservoirs, *Petroleum Exploration and Development*, vol.36, no.2, 2009.
[33] T. W. Jiang, Z. W. Huang, J. B. Li and Y. S. Zhou, Internal flow mechanism of cone-straight nozzle, *Petroleum Science*, vol.18, pp.1507-1519, 2021.

Author Biography

Yuanlong Yue received the B.Sc. degree in automation and the Ph.D. degree in control science and engineering from China University of Petroleum (Beijing), China, in 2008 and 2014, respectively.

He is currently a senior engineer in automation at the College of Information Science and Engineering, China University of Petroleum (Beijing), China. His research interests include subsea communication protocol, highly reliable imbedded system design, and multi-sensor data fusion. He is the author or coauthor of more than 20 refereed technical papers, and he is the holder of 6 patents in his areas of interest.

Haoyang Wen obtained his Bachelor degree in automation from China University of Petroleum (Beijing), China in 2020 and he is studying for a master's degree in control science and engineering at the College of Information Science and Engineering, China University of Petroleum (Beijing).

His main work focuses on the intelligent control of oil fields, including intelligent stratified water injection, fusion control, and flow assurance.

Xin Zuo received the B.Sc. degree from East China Petroleum Institute (now China University of Petroleum (Beijing)), China, in 1984; he worked as the assistant at East China Petroleum Institute from September 1984 to August 1987; he received the Master degree in China University of Petroleum (Beijing), China, in 1990.

He is currently a full-time professor at the College of Information Science and Engineering, China University of Petroleum (Beijing), China. He is a member of Expert Committee of China National Association for Automation in Petroleum and Chemical Industry. He is the author or coauthor of more than 110 refereed technical papers, and he is the holder of 20 patents in his areas of interest. His research interests include subsea production control systems design, subsea production reliability research, process control design and real-time optimization.

Mao Sheng received his Ph.D. degree in Oil and Gas Well Engineering from China University of Petroleum (Beijing) in 2008, and is now a professor and doctoral supervisor in the College of Petroleum Engineering at China University of Petroleum (Beijing).

His research areas include unconventional oil and gas fracturing completion theory and application, and artificial intelligence for oil and gas drilling. He has published 35 papers as first and corresponding author, co-authored 3 monographs in English and Chinese, and invited 3 presentations.

Fuchao Sun graduated from China University of Petroleum (Beijing) with a Master's degree in 2007. He is now working as a senior engineer in the Institute of Oil and Gas Production Equipment, Research Institute of Petroleum Exploration and Development.

His main research area includes petroleum and natural gas engineering, with specific research interests in intelligent stratified injection and extraction technology research. He has published more than 30 papers in leading petroleum engineering or control engineering journals such as Petroleum Exploration and Development, SPE Asia Pacific Oil, and International Journal of Control and Automation.